

Title

An Integrated Clinical, Omic, and Image Atlas of an Evolving Metastatic Breast Cancer

Authors/Affiliations

Brett E. Johnson^{1,2}, Allison L. Creason^{1,2}, Jayne M. Stommel^{1,2}, Jamie Keck¹, Swapnil Parmar¹, Courtney B. Betts^{1,3}, Aurora Blucher^{1,3}, Christopher Boniface^{2,4}, Elmar Bucher², Erik Burlingame^{2,5}, Koei Chin^{1,2}, Jennifer Eng², Heidi S. Feiler^{1,2}, Annette Kolodzie¹, Ben Kong^{1,6}, Marilynne Labrie^{1,3}, Patrick Leyshock¹, Souraya Mitri¹, Janice Patterson^{1,7}, Jessica L. Riesterer^{2,8}, Shamilene Sivagnanam^{1,3,5}, Damir Sudar⁹, Guillaume Thibault², Christina Zheng¹, Xiaolin Nan^{2,4}, Laura M. Heiser^{1,2}, Paul T. Spellman^{2,10}, George Thomas^{1,11}, Emek Demir^{1,10}, Young Hwan Chang^{2,5}, Lisa M. Coussens^{1,3}, Alexander R. Guimaraes^{1,12}, Christopher Corless^{7,11}, Jeremy Goecks^{1,2}, Raymond Bergan¹³, Zahi Mitri^{13,14}, Gordon B. Mills^{1,3}, and Joe W. Gray^{1,2,*}

¹Knight Cancer Institute, Oregon Health & Science University, Portland, OR, 97239, USA

²Department of Biomedical Engineering, Oregon Health & Science University, Portland, OR, 97239, USA

³Department of Cell, Developmental & Cancer Biology, Oregon Health & Science University, Portland, OR, 97239, USA

⁴Cancer Early Detection Advanced Research Center, Oregon Health & Science University, Portland, OR, 97239, USA

⁵Computational Biology Program, Oregon Health & Science University, Portland, OR, 97239, USA

⁶Department of Pharmacy Services, Oregon Health & Science University, Portland, OR, 97239, USA

⁷Knight Diagnostic Laboratories, Oregon Health and Science University, Portland, OR, 97239, USA

⁸Multiscale Microscopy Core, Oregon Health & Science University, Portland, OR, 97239, USA

⁹Quantitative Imaging Systems LLC, Portland, OR, 97239, USA

¹⁰Department of Molecular and Medical Genetics, Oregon Health & Science University, Portland, OR, 97239, USA

¹¹Department of Pathology & Laboratory Medicine, Oregon Health & Science University, Portland, OR, 97239, USA

¹²Department of Diagnostic Radiology, Oregon Health & Science University, Portland, OR, 97239, USA

¹³Division of Hematology & Medical Oncology, Knight Cancer Institute, Oregon Health & Science University, Portland, OR, 97239, USA

¹⁴Department of Medicine, Knight Cancer Institute, Oregon Health & Science University, Portland, OR, 97239, USA

Author List Footnotes

Further information and requests for resources and reagents should be directed to and will be fulfilled by the Lead Contact, Joe Gray (grayjo@ohsu.edu).

Contact Info

Correspondence: grayjo@ohsu.edu

Summary

Metastatic cancers often respond to treatment initially but almost universally escape therapeutic control through molecular mechanisms intrinsic to tumor cells, as well as extrinsic influences from immune cells, stroma, and structural microenvironments. We explore the extent to which we can learn these mechanisms and associated therapeutic vulnerabilities by linking

comprehensive molecular and multiscale imaging analyses of tumor biopsies to detailed clinical information for a patient with metastatic breast cancer. Our analyses of three serial biopsies include DNA, RNA, and protein profiling, plus quantification of tumor microenvironment composition using multiplex immunostaining and electron microscopy. Features from these analyses are linked to treatments and treatment-response measurements, including CT and PET images, circulating tumor DNA and tumor protein levels in blood, and treatment-limiting readouts of blood counts and liver function. Importantly, the measurement modalities unique to this study complemented routine diagnostics to suggest actionable mechanisms of response and resistance for each treatment phase.

Keywords

metastatic breast cancer, precision oncology, personalized medicine, human tumor atlas.

Introduction

Precision Medicine is an approach to disease management in which treatments are selected based on the presence of one or more molecular, environmental, or lifestyle features that are associated in cohort studies with a positive therapeutic response. Applied to cancer, this approach has led to substantial improvements in outcomes for a subset of patients by using powerful analytical procedures to select patients carrying biomarkers whose presence is associated with an increased likelihood of responding. These biomarkers can be genomic or epigenomic abnormalities that activate signaling pathways on which cancers depend for survival, regulatory networks that control therapeutically-vulnerable cancer “hallmarks”, microenvironmental architectures, or immune dysfunctions that can be rectified by treatment with checkpoint inhibitors or immune stimulators.

Unfortunately, treatments deployed according to precision medicine principles do not always elicit positive responses even in patients with guiding biomarkers, and durable control is not achieved for the majority of patients with metastatic cancer. We posit that the failure to control individual cancers using biomarker-guided treatments stems from our imperfect understanding of critical aspects of individual tumors and the patients in which they manifest. These mechanisms may involve regulatory networks intrinsic to tumor cells, chemical and mechanical signals from proximal or distal microenvironments, and/or aspects of immune system dysfunction. These mechanisms may vary between patients, across metastases within a patient, and among tumor cell subpopulations within a single lesion, and they may change during treatment.

We describe here our efforts to identify these mechanisms through a robust N-of-1 analysis of a patient with metastatic, hormone receptor-positive breast cancer. We used a diverse array of molecular, microscopic, and quantitative techniques to analyze this patient’s primary tumor and three metastatic lesions in three therapeutic phases over 42 months, and the data were linked to multiple clinical parameters. The resulting data and integrative analyses were then used to generate an Omic and Multidimensional Spatial (OMS) Atlas comprised of the combined clinical and tumor biological data. The clinical data include 1) precise information about drug doses, treatment times, and mechanisms of action; 2) therapeutic efficacy measures that approximate tumor size by computed tomography (CT) and metabolic activity by fluorodeoxyglucose-positron emission tomography (FDG-PET); and 3) tumor protein biomarkers and circulating tumor DNA (ctDNA) levels in blood. The tumor biological data together describe the cellular and molecular composition and organization of the multiple biopsies, and include: 1) comprehensive DNA, RNA, and protein profiles; 2) molecular signaling pathways and transcriptional regulatory networks; 3) immune, stromal, and tumor cell composition and organization; and 4) 2D and 3D subcellular and extracellular ultrastructure. Both the clinical and biological studies were carried out under the Serial Measurements of Molecular and Architectural Responses to Therapy

(SMMART) program at Oregon Health & Science University (OHSU; (Mitri et al., 2018)) with support from the Human Tumor Atlas Network (HTAN; (Rozenblatt-Rosen et al., 2020)). All the data are available through the HTAN Data Coordinating Center (<https://humantumoratlas.org/>) to encourage community participation and further analysis.

In the following sections, we describe the resulting integrative OMS Atlas in which data from metastatic tumors from a single patient are compared to each other and to other breast tumors in The Cancer Genome Atlas (TCGA). We include the clinical and experimental workflows used to acquire and manage the data and highlight patterns of non-linear clonal evolution that generated clinically-relevant genetic heterogeneity among biopsies. We also describe how our multi-faceted analytical approaches revealed aspects of the tumors' cellular and subcellular compositions and organizations that inform on cancer biology and therapeutic response, and we present examples of putative response and resistance mechanisms by comparing lesion characteristics and quantitative response metrics to published biomedical literature and datasets catalogued by the TCGA and HTAN. To our knowledge, this is the most comprehensive analysis of the response of a human cancer to treatment that has been generated to date. We show the feasibility of generating a wealth of omic and multiscale image data on individual biopsies rapidly enough to influence the treatment of a patient and the value of considering drug treatments as tumor perturbations that can inform on mechanisms of response and resistance. Finally, our results reveal a strategy that can be used to achieve more durable and tolerable control of metastatic cancers by quickly adjusting treatments to counter resistance mechanisms as they arise. Overall, we demonstrate an approach to Personalized Medicine in which the knowledge gained from decades of fundamental cancer biology and precision medicine are applied to the treatment of an individual cancer patient.

Results

Workflows for the implementation of Personalized Medicine.

We established the SMMART program and HTAN workflows for rapid collection and interpretation of information about treatments, tumor responses, and the molecular and cellular characteristics of tumor lesions in ways that can support clinical decision making and mechanistic discovery (Figure 1). All patients in this program consent to participate in the IRB-approved observational study Molecular Mechanisms of Tumor Evolution and Resistance to Therapy (MMTERT). Manual and automated abstraction of clinical metadata from the patient's medical record include precise information about treatment times and doses for each drug or radiation treatment, as well as indicators of response from anatomic imaging.

Biospecimens prospectively collected include recurring blood draws and core needle biopsies, whereby biopsy tissue is divided and preserved for each downstream assay within two to five minutes of removal from the patient. Biospecimens are used for both clinical analytics, which are performed in a CLIA-certified/CAP-accredited laboratory and are available to support clinical decision-making, and exploratory analytics, which are performed in academic research laboratories or core facilities. We integrate several software applications to create a robust computational platform for management of biospecimens as well as analysis and visualization of the resultant clinical and analytic data. Biospecimens are tracked and managed using a custom implementation of the LabVantage laboratory information management system. The LabKey system (Nelson et al., 2011) has been extended to store and visualize both clinical data and results from analysis workflows. The Galaxy computational workbench (Afgan et al., 2018) is used to create and run multi-step analysis workflows that process raw omics and imaging datasets. The OMERO system (Allan et al., 2012) is used to visualize multiplex imaging and electron microscopy datasets and associated metadata. Ultimately, patient information, clinical assay results, and analyses are presented to a multi-disciplinary clinical tumor board charged

with providing precision medicine-based recommendations for combination therapies. Final treatment selection is at the discretion of the treating physician and patient.

An integrated clinical, omic, and multiscale image atlas of metastatic breast cancer responses to treatment.

The focus of this study is a female who was diagnosed with hormone receptor-positive, HER2 normal right breast ductal carcinoma at the age of 64. She underwent a lumpectomy with intra-operative radiation therapy followed by treatment with four cycles of adjuvant docetaxel and cyclophosphamide chemotherapy. She then received two years of anastrozole treatment, followed by exemestane for five years. At that time, an ultrasound prompted by persistent abdominal discomfort revealed at least three liver masses, suggestive of metastasis. Staging CT scans revealed widespread metastatic disease involving mediastinal lymph nodes including the hila bilaterally, lung parenchyma, liver, spleen, right adrenal gland, retroperitoneal lymph nodes, and likely skeleton. An FDG-PET bone scan was positive for metastatic bone disease. The patient was then enrolled in the SMMART program and consented to the MMERT observational study (see Methods).

We developed a comprehensive omic and image-based atlas that captured the evolution of this metastatic breast cancer as the patient was treated with combinations of drugs in three phases over a 42-month period. All treatment phases included at least one drug to reduce proliferation. Phase 1 consisted of palbociclib, everolimus, and fulvestrant. Phase 2 consisted of doxorubicin and pembrolizumab. Phase 3 consisted of enzalutamide, capecitabine, fulvestrant, and the continuation of pembrolizumab. Temporary tumor control was achieved in all three phases, with a new phase of therapy beginning upon signs of progression.

This OMS Atlas links clinical metadata (Table S1) such as detailed treatment doses and timelines (Figure 2A) to tumor response measurements, including frequent measures of CEA, CA 15-3, and CA 27-29 serum tumor protein biomarker levels (Figure 2B) and lesion size and location estimates from periodic CT and FDG-PET scans (Figure 2C). Figure S1 shows representative CT, FDG-PET, and ultrasound images from key timepoints during this study. Figure S2 links the therapeutic timeline to toxicity-related blood cell composition and liver function measurements as well as ctDNA abundance.

Execution of the workflow described above enabled a detailed assessment of blood, tumor, and tumor microenvironment responses to the three phases of treatment. A liver biopsy was taken before Phase 1 began (Bx1, Liver lesion 8, Figure 2C); a biopsy of a different liver lesion was taken at the end of Phase 1 (Bx2, Liver lesion 9, Figure 2C); and a bone biopsy was taken at the end of Phase 3 (Bx3, lesion not visible by CT). The end of treatment biopsies (Bx2 and Bx3) were performed with the goal of capturing samples from lesions that were progressing while still on therapy (Figure 2A).

The molecular profiles of each biopsy generated through extensive omics and imaging assays provided a window into the mechanisms of resistance that enabled the disease to escape from treatment. They also documented the heterogeneity of the cancer, its evolution, and new therapeutic vulnerabilities that arose as the cancer evolved. Figures 3-6 summarize the results from ten distinct omic and multiscale spatial imaging assays that were used, where tissue allowed, for analyses of the primary tumor and three tumor biopsies. Table S1 includes clinically reported results of immunohistochemistry (IHC) staining. Analyses summarized in Figures 3 and S3 highlight the differences between biopsies in genetic alterations, gene expression, protein levels, and computed pathway activities. Figures 3A and 3B summarize the results of DNA analyses used to identify mutations and copy number alterations in a clinically curated panel of cancer genes (GeneTrails[®] Solid Tumor Panel) and by whole exome sequencing (WES). Figures S2E and S3A summarize the results of whole exome and Dual Index Degenerate

Adaptor Sequencing (DIDA-Seq) of ctDNA from serial blood samples (Butler et al., 2019). Figure 3 also summarizes the results from RNA sequencing (RNAseq) to characterize the whole transcriptome (Figure 3C), reverse phase protein arrays (RPPA) to profile the abundance of 450 proteins and phosphoproteins (Figures 3D, 3F; (Chen et al., 2019; Labrie et al., 2019a)), and a clinical multiplex protein analysis (Intracellular Signaling Protein Panel) of 22 cancer proteins and phosphoproteins (Figure 3E; (Lee et al., 2018)). Computed pathway activity was estimated by assessing proteomic pathway signatures (Labrie et al., 2019a), total or phosphoprotein abundance levels, transcriptomic gene set variation analysis (GSVA; (Hanzelmann et al., 2013; Liberzon et al., 2015)), and transcriptional regulator networks (see Methods). Transcript and protein levels as well as pathway activity estimates for the three biopsies were compared to other breast cancers from a TCGA cohort (TCGA BRCA; Table S2; (Cancer Genome Atlas, 2012)). Integrative analyses, including multi-omic pathway analysis, were used to explore relationships and compare changes across gene expression, transcriptional regulator activities, and protein/phosphoprotein levels between the biopsies (Figures S3D, S3E). Figures 4 and S4 show changes between the primary tumor and three metastases in the composition and functional status of individual leukocyte lineages using multiplex immunohistochemistry (mIHC; (Banik et al., 2020; Tsujikawa et al., 2017; Tsujikawa et al., 2019)). Figures 5 and S5 assess tumor and microenvironment cellular composition, functional state, and spatial organization using cyclic immunofluorescence (CyclIF; (Eng et al., 2020; Lin et al., 2015)) and focused ion beam-scanning electron microscopy (FIB-SEM; (Riesterer et al., 2020)), highlighting differences between the metastatic lesions. Figures 6 and S6A show additional two-dimensional (2D) and three-dimensional (3D) cellular and subcellular features, with potential therapeutic relevance revealed using FIB-SEM.

This OMS Atlas is deep rather than broad, focusing on a single patient over time. As an N-of-1 study, we could not use population-based statistical approaches to identify features significantly associated with therapeutic response and resistance. Instead, we used three different approaches to link this patient's molecular features to putative mechanisms of response and resistance. First, patient data were combined with curated datasets, such as TCGA, to identify tumor features that were unusually high or low compared to cohorts of similar patients. These unusual features provide a starting point for understanding what is unique in the biopsied lesion that may be driving its behavior. Second, we connected molecular features to therapeutic responses reported in domain literature and databases, such as the G2P meta-knowledgebase that associates somatic variants found in six prominent cancer variant knowledgebases with prognosis and response to therapy (Wagner et al., 2020), and curated networks obtained from the Pathway Commons database (Rodchenkov et al., 2020). Third, we identified features that changed between biopsies taken pre-treatment versus on-progression as candidate resistance mechanisms. We assigned high confidence to mechanism-associated features that were implicated by several independent approaches. Details of the assays and selected results related to aspects of tumor treatment are described in the following sections in order to elucidate potential mechanisms of response and resistance.

Genomic evolution between biopsied lesions was substantial.

We performed a comparative analysis of WES data from the primary tumor and three subsequent metastatic biopsies to understand the genomic heterogeneity and evolutionary trajectory of these lesions. A common set of copy number abnormalities was present in all three biopsies, including an amplification on chromosome 11 encompassing the CDK4/6 binding partner cyclin D1 (*CCND1*; Figure S3B), indicating that each biopsied lesion site arose from a common ancestral cell clone. Likewise, a subset of somatic mutations was identified across all four biopsies (Ubiquitous; Figures 3A, S3A). There was also a set of mutations unique to each lesion (Private), as well as a set of variants common to Bx1 and Bx2 (Shared) but absent from

Bx3. This heterogeneity between biopsies included differences in biologically-relevant mutations. For example, Bx2 contained a hotspot *PIK3CA* mutation (p.E542K; NM_006218:c.1624G>A), that was absent from the primary tumor, Bx1, and Bx3. This is a known pathogenic mutation, and its absence from Bx3 later in the course of this patient's disease indicates a non-linear pattern of genomic evolution between the sequential biopsies. To understand the pattern of clonal evolution that gave rise to the heterogeneity between the three biopsied metastatic lesions, we used the mutations identified from WES to construct a phylogenetic tree (Figure 3B). Interestingly, this analysis revealed a pattern of branching clonal evolution in which Bx3 diverged from the primary tumor at an earlier evolutionary timepoint than Bx1 and Bx2. The Bx3 metastatic lesion was not tracked by CT imaging due to its anatomical location in the spine but first appeared on FDG-PET imaging just one month before Bx3 (Figure S1G), being absent from all prior FDG-PET scans (Figures 2, S1A, S1F). These data therefore indicate that the chronological time of emergence of a detectable lesion may not be strictly related to the evolutionary history of the clone.

Bx3 was acquired from a bone lesion that progressed during combination treatment in Phase 3 with enzalutamide, pembrolizumab, fulvestrant, and capecitabine (Figure 2A). While WES did not identify any driver mutations private to Bx3 that would explain the clinically late outgrowth of this evolutionarily early tumor, it did reveal a focal, 2.3 MB, 8-copy genomic amplification on chromosome 18 (18p11.32), encoding thymidylate synthetase (*TYMS*) and the SRC family tyrosine kinase *YES1* that was not identified in prior biopsies or the primary tumor (Figures 3B, S3B). This amplification on chromosome 18 was accompanied by increased RNA expression of *TYMS* (3.6 log₂ fold) and *YES1* (1.3 log₂ fold), indicating functional consequences of the copy number increase. *TYMS*, which catalyzes the conversion of dUMP to dTMP, is the molecular target of the capecitabine metabolite FdUMP, and its over expression has been reported as a resistance mechanism to this agent (Marangoni et al., 2018). This indicates that the *TYMS/YES1* amplification may have given Bx3 a relative fitness advantage under the selective pressure of capecitabine treatment, providing a potential explanation for the temporally late emergence of a clone that branched off early in the evolutionary process (Figure 3B). *YES1* can be inhibited by the broad-spectrum kinase inhibitor dasatinib revealing a possible therapeutic strategy to counter resistance mediated by this amplification.

Genomic differences between the biopsies could be due to pre-existing genetic heterogeneity between metastases or to branching clonal evolution during therapeutic treatment. To discriminate between these possibilities, we performed WES on ctDNA collected immediately prior to Bx1 (ctDNA 1) and 23 days after Bx2 (ctDNA 2). We detected mutations previously identified as private to each of the biopsies (Figure S3A) at both ctDNA collection timepoints, indicating pre-existing genomic heterogeneity between metastases, with clones carrying advantageous alterations subsequently selected for by specific treatments.

Circulating tumor DNA increases coincided with both tumor progression and radiation therapy.

Disease progression and response over the first 32 months of treatment following enrollment in the study was also assessed by monitoring ctDNA levels from serial blood samples using DIDA-Seq for a panel of 53 single-nucleotide variants (SNVs) that were present in the patient's primary tumor and first two metastatic biopsies (Butler et al., 2019). The average variant allele frequency (VAF) of the panel of SNVs remained consistently below 0.3% of the total cell free DNA in the blood during this period, with the exception of two transient increases (Figure S2E). The first occurred immediately prior to Bx2, coincident with rising CA 15-3 and CA 27-29 and increasing radiographic size of several metastases, including the Bx2 liver lesion (Figures 2B, 2C, S2E). The increase in ctDNA VAF was greatest for the mutations that were common to the primary tumor and first two biopsies (Bx1_Bx2_Primary, 30% VAF) compared to those private to the metastases (Bx1_Bx2, 3.1%; Bx1, 0.05%; Bx2, 1.3%; Figure S2E). We hypothesize that this

variation in VAFs reflects mutational heterogeneity among the diverse metastatic lesions (Figure 2C). The second ctDNA level increase occurred after the patient began a course of palliative radiation therapy to spinal lesions at C2-C5. Interestingly, the VAFs of all SNV groups in the panel increased at this time, including those private to liver lesions Bx1 and Bx2. One possible explanation for this observation is an immune-mediated abscopal radiation effect on lesions both inside and outside the irradiated field (Liu et al., 2018). The detection of most ubiquitous mutations in the ctDNA as well as many private to Bx1 and Bx2 reaffirms the utility of the assay in detecting the emergence of clones carrying resistance-associated mutations before they grow to become a dominant population. Intriguingly, our observation that radiotherapy appears to have induced a transient increase in ctDNA abundance provides perhaps an opportunity to profile heterogeneous disease by liquid biopsy in patients who undergo radiation therapy for clinical need.

Exploration of cellular and molecular composition and organization.

It is well established that interactions between tumor and microenvironmental cells can significantly influence treatment outcomes, for example, by forming physical barriers that hinder drug and immune cell access or by providing chemical and mechanical signals altering the tumor cell drug responses and/or immune cell activity (Hanahan and Coussens, 2012). We mapped cellular states and inter- and intracellular interactions that might have influenced the observed therapeutic responses, using a combination of mIHC, CycIF, and FIB-SEM.

Immune monitoring using mIHC illustrates opportunities to increase immune surveillance.

To quantitatively evaluate composition and functionality of lymphoid and myeloid lineage cells in the primary tumor and three metastatic biopsies, we used a mIHC platform for iterative immunodetection with 23-36 antibodies reporting leukocyte lineage and effector functionality on FFPE tissue specimens, followed by a computational analysis workflow (Figure 4; Table S2) (Banik et al., 2020; Tsujikawa et al., 2017; Tsujikawa et al., 2019). These analyses revealed a modest increase in CD45⁺ immune cells in Bx1 compared to the primary tumor, a reduction in Bx2, and an ~8-fold expansion in Bx3 (Figures 4A, 4B). Analyses of the major leukocyte lineages revealed that macrophages and monocytes comprised the dominant lineage subgroup in all samples except Bx3 (Figure 4C). In deeper analysis of the myeloid lineage relative to Bx2, Bx1 contained a larger percentage of immature dendritic cells, whereas Bx2 contained increased proportions of macrophages and monocytes, with the largest increase in CD163⁺ macrophages in Bx2 (Figures 4C, 4D). CD163 positivity has been associated with differentiation of myelomonocytic cells towards an alternatively-activated or “M2” type state, an event considered to be pro-tumorigenic within solid tumors (Barros et al., 2013). CD163 expression on monocytes and macrophages is induced by IL-10 and glucocorticoids and repressed by lipopolysaccharides TNF α , and IFN γ (Buechler et al., 2000). Consistent with increased CD163 positivity, Bx2 had enriched expression of the GSVA transcriptional pathways “BioCarta IL10 Pathway”, “Reactome Interleukin 10 Signaling”, and “GO Glucocorticoid Receptor Binding”; however, pathways that negatively regulate CD163 were also enriched, including “GO Lipopolysaccharide Receptor Activity”, “TNFA Signaling Via NF κ B”, and “Interferon Gamma Response” (Figure 3C; Table S2).

Assessment of the T cell compartment indicated variable presence of total CD3⁺ T cells: Bx2 contained fewer T cells than Bx1, but these were further increased (relatively) in Bx3 as compared to Bx2 (Figure 4E). The primary tumor contained a higher percentage of CD3⁺CD8⁺ T cells than CD3⁺CD4⁺ helper T cells, which was not observed in any of the biopsies (Figure 4E). Only a small fraction of CD3⁺CD4⁺ and CD3⁺CD8⁺ T cells in either the primary or Bx1 tumor expressed the programmed cell death-1 (PD-1) protein, typically expressed on activated T cells following persistent antigen exposure (Figure 4F; (Pauken and Wherry, 2015)). From a

treatment perspective, low expression of PD-1 and low overall abundance of CD3⁺CD8⁺ T cells and CD163⁺ macrophages in the primary tumor and Bx1 likely indicate that neither had initiated a T cell-mediated immune response. Thus, in Bx1 there was little evidence to support the utility of checkpoint inhibitors targeting the PD-1/PD-L1 axis in Phase 1.

The T cell status was markedly altered in Bx2 (Figures 4C, 4G, 4H). Notably, while T cells were less abundant in Bx2 compared to Bx1, a larger fraction of CD3⁺CD4⁺ and CD3⁺CD8⁺ T cells expressed PD-1 in Bx2 (Figure 4F) coincident with a relatively reduced presence of FoxP3⁺CD4⁺ Tregs and expanded population of Th17 CD4⁺ T cells (Figure 4H). Th17 T cells and Tregs arise from a common precursor but with opposing functionality upon terminal differentiation, with Th17 cells promoting and Tregs dampening antitumor immunity (Knochelmann et al., 2018). Interestingly, there are reports indicating that anti-estrogens also inhibit CD4⁺CD25⁺ Treg differentiation (Adurthi et al., 2017; Tai et al., 2008). Using PD-1 and eomesodermin (EOMES) expression to further audit CD8⁺ T cell functional status, we found that EOMES⁺ populations were expanded in Bx2, whereas PD-1⁺EOMES⁺ cells were reduced (Figure 4G). EOMES is a T-box transcription factor that regulates protein expression for T cell memory and upregulates T cell inhibitory receptors; however, in some tumors (liver), dysfunctional T cells exhibit reduced EOMES (and T-bet) expression (Schietinger et al., 2016), thus also supporting the hypothesis that dysfunction of these T cells might be arrested by PD-1-blockade.

The immune ecosystem changed again dramatically between Bx2 and Bx3; yet, it is important to note a change in location of the metastasis from liver to bone. The dominance of CD163⁺ myeloid cells was greatly reduced, replaced with granulocytes, dendritic cells, and an expansion of CD20⁺ B cells and CD3⁺ T cells. Both CD3⁺CD4⁺ and CD3⁺CD8⁺ T cells displayed PD-1 expression, potentially indicative of their recent activation but not necessarily indicative of effective anti-tumor functionality. Further, granulocytes, encompassing basophils, eosinophils, and neutrophils, were also expanded in presence. Neutrophils in particular can harbor suppressive effects on T cells and are associated with poor prognosis in many solid tumors, including breast cancer (Hanahan and Coussens, 2012). Moreover, a high neutrophil-to-lymphocyte ratio (NLR) has been found to be a poor prognostic indicator in breast cancer (Ethier et al., 2017). Although Bx3 displayed an NLR of ~0.8 (data not shown), which is not classified as high (1.9-5 range), suppressive activity could be present. Further, only 4.7% of the dendritic cells in Bx3 expressed DC-LAMP/CD208, a lysosomal protein involved in processing and presenting antigen and indicative of DC maturation, which is necessary for naïve T cell priming. Thus, lack of support for existing T cells or active suppression likely contributed to disease progression. The existence of immature DCs present therapeutic avenues to pursue, including the opportunity to drive DC maturation with alternative forms of immune therapy, such as GM-CSF vaccination (GVAX), DC agonists including CD40, and small molecule inhibitors including JAK/STAT and MAPK inhibition, and/or “re-invigorating” T cells (Wculek et al., 2020).

Tumor and stromal responses to therapy revealed using CyclF.

We used a CyclF analysis platform with probes for 20 proteins as previously described (Eng et al., 2020; Lin et al., 2015) to assess the tumor and stromal composition and organization of all three biopsied metastatic lesions (Table S2). To enable subpopulation analysis within the context of known biology for this luminal breast cancer (Figure S3C), we included control biospecimens prepared from normal breast tissue, tonsil, an unrelated luminal HER2 breast cancer, and six cell lines representing basal (HCC1143, HCC3153), claudin-low (MDAMB436), luminal (T47D), and HER2 positive (BT474, AU565) breast cancers. Collective analyses of these tissues and cell lines defined three stromal and eight tumor subpopulations (Figures 5A, 5C, S5A). Three of the stromal clusters (clusters 3, 4, and 7) and three of the tumor clusters (clusters 6, 9, and 10) were represented as major subpopulations in Bx1, Bx2, and Bx3 (Figures 5C, S5A). The stromal clusters were identified as endothelial cells expressing CD31, fibroblast-

like cells expressing high levels of VIM/aSMA, and immune cells expressing CD45, CD4, CD8, and/or CD68. The tumor clusters were identified as expressing CK7/CK19, with differential expression of ER, PCNA, and Ki-67. Comparative analyses of the biopsies showed that the fraction of tumor cells expressing high levels of ER and PCNA (cluster 10) increased in Bx3 (Figure 5C), possibly reflecting an increase in PCNA dependent DNA repair (Li et al., 1994). Of course, differences between the anatomical locations of Bx3 (bone, Figure S1A) and Bx1 and Bx2 (liver, Figures S1F, S1G) could also explain differences between these metastases.

Visual review of the CycIF images revealed a reduced tumor-to-stromal cell ratio in Bx2 compared to Bx1 and Bx3 (Figures 5B, S5B) that was reflected in a cellular composition analysis (Figure S5C). Interestingly, Bx2 also displayed the highest subpopulation cluster heterogeneity among the biopsies (Figure S5C). The lower metabolic activity of stromal cells in Bx2 compared to Bx1 likely explains why FDG-PET activity decreased after Bx2, while lesions sizes measured by CT decreased only modestly (Figures 2C, S1F). Quantitative measures of distances from each tumor cell to the nearest macrophage, T cell, endothelial cell, and fibroblast showed differences between the stromal cell types (Figure 5D). Fibroblasts were in close proximity to tumor cells in all biopsies, thereby presenting the opportunity to impact therapeutic response (Paraiso and Smalley, 2013). Endothelial cells were in closer proximity to the tumor cells in Bx2 than Bx1 and in closer proximity in Bx3 than Bx2. In Bx3, the tumor cells were as close to the endothelial cells as to the fibroblasts. Macrophages were slightly farther from tumor cells than the fibroblasts were to tumor cells in Bx1 and Bx2 but were generally several cell diameters away from tumor cells in Bx3. T cells, on the other hand, were located many cell diameters from the nearest tumor cell in all biopsies, thereby reducing the probability of T cell mediated cell killing in all biopsies.

Visual analysis also revealed that the endothelial, fibroblast, and immune cells were co-localized in each biopsy and spatially organized around but excluded from neoplastic tumor cells, which themselves were organized in nests (Figure 5B). This architecture possibly formed a chemical and mechanical barrier to chemical and immune attack and was explored further using FIB-SEM as described below.

Therapy related inter- and intracellular compositions and interactions revealed using FIB-SEM.

We explored the ultrastructure of inter- and intracellular interactions in large format 2D and targeted 3D images acquired using FIB-SEM as previously described (Riesterer et al., 2020), with emphasis on aspects of nanobiology that might affect therapeutic response. Computational renderings of the 3D images were particularly informative in Bx1 (Movies S1, S2) and Bx2 (Movie S3). Insufficient material was available from Bx3 to allow EM analysis.

The ~4 nanometer resolution 3D FIB-SEM Movie S3 and selected views in Figure 5E reveal details of intercellular interactions between tumor and stromal cells that cannot be appreciated from images generated using light microscopy. These images confirm the organization of stromal cells around tumor clusters in Bx1 and Bx2 (Figures S6A, 5E). However, they reveal an intricate interaction pattern between tumor and stromal cells that indicates the stromal barrier may be formed as a result of active communication between the tumor and stromal cells. The 3D images show a remarkable degree of biological and mechanical heterogeneity that should be assessed for functional impact in experimental models. In particular, these images show the robust manifestation of ~100 nm diameter, micrometers long filopodia-like protrusions (FLPs) that appear to establish interactions between tumor cells and between the tumor and the stromal microenvironment (Figure 6A-C, Movie S2). The abundance of FLPs is somewhat increased in Bx2 compared to Bx1 (Figure 6G, Movies S1-3). Published work (Kerber and Cheney, 2011) and our own studies in model systems show that these protrusions have an actin-rich core, are decorated with receptor tyrosine kinases, and are dependent on the actin-

motor protein Myosin-X encoded by the gene *MYO10*. Dynamic *in vitro* images acquired using stochastic optical reconstruction microscopy (STORM) show that cultured SKBR3 breast cancer cells respond to cytokines like EGF by rapidly decreasing protrusion length in ways that cause cells to move toward the anchored ends of the protrusions (Figure S6B, Movie S4). This indicates the possibility of protrusion-mediated signaling whereby the long and dynamic FLPs could mediate both proximal and distal interactions and directed movement. Published studies also suggest the possibility that FLPs mediate protein transport between cells (Desir et al., 2018).

The 3D movies of FIB-SEM images of cancer cells in Movies S1-3 also provide important information about intracellular structures and interactions that may influence cell function and therapeutic response. For example, Movie S2 and Figures 6A and 6D from Bx2 show mitochondria aligned along the length of an elongated cell and insinuated into nuclear folds, thereby increasing the potential for nuclear-mitochondria signaling. The resulting increased mitochondria-nucleus proximity might alter aspects of DNA damage repair and/or ROS signaling (Ogawa and Baserga, 2017; Saki and Prakash, 2017). We speculate that the alignment of the mitochondria along the long axis of the cell and the close association of mitochondria with the nucleus resulted from forces generated as the cells moved through a dense microenvironment, as suggested by the dynamic model system studies described above and illustrated in Figure S6B and Movie S4.

Movies S1 and S2 and Figures 6C, 6E, and 6F depict a high abundance of lamellipodia and macropinosomes, indicating nutrient scavenging via macropinocytosis as a possible tumor survival mechanism (Commisso et al., 2013; Hosios et al., 2016). Macropinocytosis is a non-selective endocytosis process that enables the uptake of nutrients and proteins from the intercellular space, including those from nearby dying cells (Commisso et al., 2013). Uptake is mediated by actin-rich lamellipodia that engulf and internalize extracellular materials. This process has been implicated as a survival mechanism in Ras-transformed cells in amino acid-poor environments (Palm et al., 2015), and it is noteworthy that the GSVA Cancer Hallmark gene set “KRAS Signaling Up” and multiple Reactome gene sets for amino acid biosynthesis are enriched in Bx2 (Figure 3C; Table S2). We speculate that drug uptake by macropinocytosis might explain the strong response to liposomal doxorubicin during Phase 2 treatment.

Movies S1 and S2 and Figure 6E show a high prevalence of densely stained vesicles in Bx2 that appear to be lysosomes, in contrast to the smaller electron-lucid macropinosomes. These acidic vesicles are known to accumulate weak bases, including some cancer drugs, via a process called lysosomotropism. In this process, basic drugs become protonated and trapped within the acidic interior of lysosomes (Villamil Giraldo et al., 2014). Analysis of 2D EM images show that the frequency of these vesicles is qualitatively higher in Bx2 compared to Bx1 (Figures 6G, S6A), and, as discussed below, may be contributing to an attenuated response to small-molecule therapeutics at the time of this biopsy.

Figure 6G presents a qualitative summary of the prominence of the nanoscale features described above in Bx1 and Bx2 made by visual analysis of large format 2D SEM images (Figure S6A) and informed by 3D FIB-SEM images of selected features as described above.

Mechanisms of therapeutic response and resistance revealed by integrative analyses.

The diverse clinical and experimental data collected from serial biopsies taken during the course of treatment are intended to support integrative analyses that reveal mechanisms of resistance and response. Full exploration of these mechanisms is beyond the scope of this paper. Instead, we present illustrative results from a comparative analysis of Bx1 (taken prior to Phase 1 treatment) versus Bx2 (taken upon progression on Phase 1 treatment) that demonstrate the

extent to which resistance and response mechanisms to Phase 1 treatment with palbociclib, everolimus, and fulvestrant (Figure 2A) can be understood.

Evidence for tumor growth despite continued drug target suppression at the time of Bx2.

The overall tumor burden and the lesion sampled in Bx2 initially regressed by radiological imaging (Figure 2C) and assessment of blood biomarkers (Figure 2B) on Phase 1 treatment but then began progressing after about 6 months. Bx2 was taken approximately 9 months after Phase 1 treatment began (Liver lesion 9, Figures 2C, S1E). Despite the increasing size of this lesion, the cell proliferation marker Ki-67 was reduced in Bx2 compared to Bx1 (20.7% vs. 25.9-31%; Table S1), and RNA and protein analyses derived from Bx2 indicated that pathways targeted by these drugs were downregulated. For example, MSigDB Cancer Hallmarks derived from GSVA of RNA expression showed that “Estrogen Early,” “Estrogen Late,” “E2F Targets,” and “MTORC1” pathways were decreased in Bx2 relative to Bx1, indicating continued activity of fulvestrant, palbociclib, and everolimus, respectively (Figure 3C). Moreover, decreases in CDK4, CDK6, and E2F1 transcriptional regulator activities (Figures S3D, S3E; Table S2) and the RPPA cell cycle protein pathways “G0-G1” and “G1-S” (Figures 3D, S3E) were consistent with response to palbociclib. Because this drug combination was no longer inhibiting this lesion, we used the OMS Atlas to investigate possible acquired resistance mechanisms and new therapeutic vulnerabilities that affect processes outside of canonical pathways. We present below illustrations of evidence gleaned from the OMS Atlas with the strongest connection to therapeutic response, acknowledging the difficulty of pinpointing the cellular and molecular changes to any single drug in a multi-drug regimen.

A PIK3CA mutation may contribute to resistance to multiple Phase 1 therapies.

We identified a *PIK3CA* p.E542K mutation in Bx2 that was not detected in the primary tumor, Bx1, or Bx3, indicating this mutation may have emerged due to selective pressure from one or more Phase 1 therapies. Indeed, this variant was among the SNVs monitored in serial blood samples by DIDA-Seq (Figure S2E) and was only detected in the ctDNA significantly above background after month 7 (0.06% VAF, $p=0.0071$, Weitzman overlapping coefficient). This is a helical-domain hotspot mutation implicated in resistance to diverse agents and in multiple tumor types and, as described below, can affect the response to any of the three Phase 1 drugs. Bx2 had evidence of PI3K pathway activation upstream of mTOR, including increased phosphorylation of AKT and AKT substrates GSK3A/B (S21/S9 phosphorylation, 1.6-fold vs. Bx1), TSC2 (T1462 phosphorylation, 1.4-fold), and MDM2 (S166 phosphorylation, 2.0-fold) (Figure 3F). While this mutation being private to Bx2 may indicate a drug resistance-related mechanism for its emergence, the co-administration of multiple drugs that target diverse but overlapping pathways made it difficult to attribute its selection to any single drug.

Escape from everolimus through mTORC1/2 feedback loops.

The mTORC1 complex inhibitor everolimus was chosen in Phase 1 treatment based on clinical trials demonstrating this drug’s efficacy in combination with endocrine therapies in treating ER positive metastatic breast cancer in patients who progressed on aromatase inhibitors, as was the case with this patient (Massarweh et al., 2014). mTORC1 is activated through inhibitory phosphorylation of its negative regulator TSC1/2 by the PI3K/AKT and RAS/MAPK pathways. This leads to multiple cell growth-promoting effects, including increased protein translation, lipid synthesis, and autophagy inhibition (Kim and Guan, 2019). Bx1 had evidence of mTORC1 activation, including high levels of S6 ribosomal protein S240/244 phosphorylation (Figure 3F) and enriched transcriptional gene sets involved in protein translation (Table S2). Bx2 showed evidence for everolimus-mediated inhibition of the mTORC1 complex, including decreased S6 phosphorylation at both S235/236 and S240/244 (0.7- and 0.2-fold vs. Bx1, respectively), as well as a decrease in the GSVA transcriptional Cancer Hallmark “MTORC1” (Figures 3C, 3F).

However, the RPPA protein pathway “TSC-mTOR” did not significantly change in Bx2 (Figure 3D), indicating this tumor may have activated everolimus bypass mechanisms that maintain oncogenic signaling in the presence of this agent.

One possible bypass mechanism is mTORC2/AKT-mediated compensatory feedback signaling, which is known to maintain oncogenic signaling in the presence of rapalogs, such as everolimus (Figure 3G; (Mi et al., 2015; O'Reilly et al., 2006)). mTORC2 is functionally distinct from mTORC1 and insensitive to everolimus. Bx2 had multiple markers of mTORC2 and AKT activation. For example, phosphorylation of AKT at S473, an mTORC2 kinase site, was increased in Bx2 relative to Bx1 (2.5-fold), and, as mentioned above, multiple AKT downstream effectors were phosphorylated (Figure 3F). AKT is also constitutively phosphorylated at this site in cells harboring oncogenic PI3K mutants, including *PIK3CA* p.E542K (Kang et al., 2005), indicating a role for this mutation in reducing everolimus efficacy in Bx2. The combined observations of decreased phospho-S6 at S240/244 and increased phospho-AKT at S473 are consistent with inhibition of mTORC1 and consequent compensatory activation of AKT by mTORC2 to maintain tumor growth in the presence of everolimus.

Activation of CDK2 and drug sequestration via lysosomotropism may contribute to resistance to palbociclib.

The cell cycle inhibitor palbociclib was given in Phase 1 treatment to counter the proliferative dysregulation indicated by a high frequency of Ki-67 positive tumor cells and amplification of the CDK4/6 binding partner *CCND1* observed in Bx1 (Table S1; Figures 3B, S3B; (Spring et al., 2020)). Palbociclib is an FDA-approved inhibitor of the cyclin D-dependent kinases CDK4 and CDK6 and has no significant activity against other CDKs. RB1 phosphorylation by CDK4/6 in early G1 and CDK2 in late G1 and early S cell cycle phases results in its release from the transcription factor E2F, enabling the transcription of genes that promote cell cycle progression (Sherr et al., 2016). Bx1 was positive for RB1 phosphorylated at S807 and S811, markers of high CDK4/6 kinase activity indicating possible susceptibility to palbociclib (Figure 3F). Indeed, serum tumor biomarkers and CT measurements decreased for the first six months on this and the other Phase 1 drugs (Figures 2B, 2C). However, RB1 phosphorylation at S807 and S811 was also found in Bx2 (1.0-fold vs. Bx1; Figure 3F), indicating possible loss of palbociclib efficacy at this time.

The RB1 phosphorylation observed in Bx2 while on palbociclib might have occurred via activation of CDK2. CDK2 activation can occur through both canonical and non-canonical mechanisms, each potentially involving oncogenic signaling through *PIK3CA* p.E542K (Figure 3H). Canonical binding of CDK2 to cyclin E is required for the G1-S transition and is inhibited by the CDK inhibitor p21 (Sherr et al., 2016). Cells lacking p21 are incapable of cell cycle arrest in response to CDK4/6 inhibitors due to dysregulated activation of CDK2/cyclin E (Herrera-Abreu et al., 2016; Iida et al., 2019; Vilgelm et al., 2019). Bx2 expressed less p21 protein than Bx1 (0.5-fold, Figure 3F), which could be due to downregulation by activated PI3K/AKT, as this pathway keeps p21 levels low in CDK4/6 inhibitor resistant cells (Vilgelm et al., 2019). AKT phosphorylation was higher in Bx2 than Bx1 (S473, 2.5-fold; T308, 1.2-fold; Figures 3F, S3D, S3E), possibly due to *PIK3CA* mutation or feedback activation of mTORC2 in response to everolimus. Tumor cells can also adapt to palbociclib via non-canonical binding of CDK2 to cyclin D1, which occurs in cells with high cyclin D1 protein levels and activated PI3K signaling (Herrera-Abreu et al., 2016). Bx2 had increased cyclin D1 protein levels (1.6-fold vs. Bx1; Figures 3F, S3D, S3E) and increased AKT activity driven by mutated *PIK3CA* as an additional palbociclib resistance mechanism (Figure 3H).

Sequestration of palbociclib via lysosomotropism may also have contributed to reduced palbociclib efficacy in Bx2. This mechanism is suggested by the increase in lysosomes from Bx1

to Bx2 revealed by FIB-SEM (Figures 6G, S6A). Drug sequestration via lysosomotropism has been implicated as a mechanism of resistance to palbociclib and other CDK4/6 inhibitors, indicating a possible role for these abundant vesicles in reducing therapeutic efficacy in this patient (Fassl et al., 2020; Llanos et al., 2019).

Signaling through the androgen receptor may enable escape from therapeutic control by fulvestrant.

Fulvestrant is a selective estrogen receptor degrader that is FDA-approved in combination with palbociclib to treat metastatic, HR-positive breast cancer in patients who have progressed on prior endocrine therapies. Its mechanisms of action include competitive inhibition of estradiol binding and induction of an ER conformational change that leads to its proteasomal degradation (Wijayarathne and McDonnell, 2001; Wittmann et al., 2007). This patient had previously progressed on anastrozole and exemestane, was ER positive in Bx1 (> 95%; Table S1), and had no *ESR1* mutations, making her a suitable candidate for this therapy. The absence of genetic alterations in *ESR1* despite multiple years of prior treatment with two aromatase inhibitors, anastrozole (two years) and exemestane (five years), is noteworthy as resistance-associated mutations in this gene are frequently reported in response to these drugs (Robinson et al., 2013; Toy et al., 2013). Bx2 showed continued ER positivity by IHC (>95%; Table S1), increased ER protein levels by RPPA (1.8-fold; Figures 3F, S3D, S3E), essentially all tumor cells expressing ER on CyclIF analysis (Figure 5C, S5D), and no mutations in *ESR1*. None of these factors indicate a possible mechanism of resistance to fulvestrant. This motivated OMS Atlas analyses to determine possible fulvestrant-resistance mechanisms in Bx2 that were independent of the estrogen receptor.

Several lines of evidence indicated androgen receptor (AR) signaling as a compensatory mechanism for ER pathway inhibition in Bx2. This biopsy was AR positive by clinical IHC (66%; Table S1), and RPPA analyses showed a dramatic increase in AR protein levels in Bx2 relative to Bx1 (5.5-fold; Figures 3F, S3D, S3E). In addition, transcriptional regulator activity measurements showed an increase in breast cancer-specific AR downstream targets (Figure S3D; Table S2). Interestingly, the Hormone Signaling Pathway as measured by RPPA was not significantly changed between these biopsies despite multiple omics analyses showing a decrease in ER activity and an increase in AR, providing further evidence that AR may have supplanted ER to maintain downstream hormone-dependent gene transcription (Figures 3C, 3D). This could have occurred through direct transcriptional activation of common target genes, as many promoters with estrogen response elements also contain binding sites for AR (Need et al., 2012). The possibility of reliance on AR signaling in the lesion sampled in Bx2 supported addition of the anti-androgen enzalutamide in Phase 3 treatment (Figure 2).

Discussion

A key goal in the OHSU SMMART and HTAN programs is to improve treatments for metastatic cancers in individual patients by identifying and opportunistically acting on therapeutic vulnerabilities and mechanisms of resistance as they present before and during extended treatments. This report describes our efforts to accomplish that by analyzing blood and tumor biospecimens as well as anatomic tumor images collected over a 42-month period from a patient with metastatic, ER+ breast cancer. Integration of these data with clinical information, including individual treatment times and doses, constitutes an Omic and Multidimensional Spatial (OMS) Atlas that we analyzed to identify mechanisms of response and resistance. We believe that this OMS Atlas constitutes the most comprehensive analysis of the response of metastatic tumors to longitudinal combination therapies reported to date.

The process workflow described in Figure 1 was critical to this atlas. This workflow brings together detailed clinical information with analysis results from complex computational

workflows. Only when this information is combined can the detailed study described in this report be carried out. Collecting and organizing needed clinical information in a timely manner is quite challenging because these data reside in multiple databases and in data formats that were not designed to provide the required level of detail or accuracy. Clinical data collection and organization was accomplished using a combination of automated and manual extraction and careful human curation. Analysis of omics and imaging data collected from blood and tumor biopsies required integrating multiple software systems for data management, processing, and visualization. Further, each of the software components was extended to meet the unique needs of our approach. Together, this process workflow outlines the many essential steps and software needed to collect and process all data quickly enough to be used for treatment decisions.

The acquisition of tissue biopsies from specific lesions combined with CT/PET imaging over time provided precise information about the behavior of each biopsied lesion before and after biopsy. This enabled direct assessment of the efficacy of treatments suggested by analyses of the biopsied lesion. Rapid preservation (two to five minutes from biopsy to start of preservation) enabled optimal conservation of the molecular and architectural features in each biopsied lesion, some of which may change within minutes after interruption of blood flow. Rapid preservation is particularly valuable in analyses of pharmacokinetic responses to drugs and in studies of nanoscale inter- and intracellular compositions and interactions.

Integrated analyses of the omic and multiscale image measurements with associated clinical treatment and response information provided information about tumor evolution over time and across treatments that enabled identification of potential mechanisms of response and resistance for each treatment phase. We accomplished this by first linking the information comprising the OMS Atlas for each biopsy with curated public datasets and domain literature that identified mechanistic associations and then identifying features that changed between biopsies taken before and during treatment. We assigned highest confidence to mechanisms that were implicated by more than one line of evidence. Identification of potential mechanisms underlying resistance was complicated by the fact that combinations of drugs were used in each phase of treatment. In retrospect, introduction of the drugs stepwise would simplify mechanistic studies by allowing the response to each to be assessed independent of the others, although this must be balanced against the need to achieve tumor control quickly. Nonetheless, several potential mechanisms of resistance and therapeutic vulnerabilities were identified for each treatment phase. Importantly, each of the analytical modalities contributed to these insights. These mechanisms and vulnerabilities are summarized below based on both clinical and research data. It is important to note that the research data were not used to guide treatment and are presented here *post hoc* to inform on possible mechanisms.

Efficacy of Phase 1 treatment with fulvestrant, palbociclib, and everolimus was compatible with ER expression, wild type *ESR1*, phosphorylated RB1, amplification of *CCND1*, and active PI3K signaling in Bx1. The treatment was initially modestly effective in reducing tumor lesion sizes and tumor protein levels in the blood, but this benefit was lost after six months. Analysis of Bx2, taken while the patient was still on Phase 1 treatment, to identify resistance mechanisms was complicated by the fact that these drugs target overlapping and interacting regulatory processes. Nonetheless, our analyses implicated upregulation of PI3K signaling via a *PIK3CA* p.E542K activating mutation, compensatory feedback signaling through mTORC2, activation of CDK2, sequestration by lysosomotropism, and compensatory signaling via the androgen receptor as possible resistance mechanisms. These analyses support switching from palbociclib to abemaciclib to counter the observed CDK2 activation (Hafner et al., 2019), use of enzalutamide to counter possible androgen mediated signaling as was done in Phase 3, and administration of a lysosomotropic drug such as hydroxychloroquine (Fassl et al., 2020) to

counter sequestration of palbociclib or abemaciclib. Phase 1 treatment was terminated when blood biomarkers and CT measurement of several—but not all—metastatic lesions began to increase sharply.

Phase 2 treatment was comprised of liposomal doxorubicin and pembrolizumab and resulted in an immediate and dramatic reduction in tumor protein biomarkers in the blood and in the sizes of several lesions, including the one sampled in Bx2. This positive response to liposomal doxorubicin was consistent with reliance of the tumor on macropinocytosis for survival, a mechanism that could also facilitate uptake of the liposomal drug composition. A positive response to the immune checkpoint inhibitor is consistent with a palbociclib mediated transcriptional upregulation of regulatory networks in Bx2 that would enhance antitumor responses, including the observed increase in CD163⁺ macrophages and the Th17/Treg ratio. These changes were accompanied by an increase in PD-1⁺ EOMES⁻ T cells that might blunt an immune response and that we speculate was attenuated by pembrolizumab. The Phase 2 treatment began to lose efficacy after approximately 6 months. This loss of efficacy plus a clinical concern for doxorubicin-mediated cardiotoxicity motivated termination of the Phase 2 treatment.

Phase 3 treatment was comprised of continued pembrolizumab plus enzalutamide, capecitabine, and fulvestrant, which resulted in a reduction in tumor biomarkers in the blood to near background levels and continued reduction in the sizes of most metastatic lesions. Enzalutamide was included to counter possible androgen receptor mediated signaling. Response to capecitabine was expected given the observation of normal levels of *TYMS*, the target of the capecitabine metabolite FdUMP. A slow rise in tumor biomarkers in the blood after approximately 20 months and the development of a persistent FDG-PET positive lesion in the bone motivated acquisition of Bx3. Analyses of that biopsy revealed a narrow amplification of the region of the genome around *TYMS*, coupled with over expression of this gene, indicating this copy number alteration as a potential resistance mechanism. Importantly, the region of amplification also contained the SRC family tyrosine kinase *YES1*, which might further contribute to tumor progression, thus indicating the possible utility of the *YES1* inhibitor dasatinib in countering resistance potentially mediated by this amplification. The multiscale imaging analyses also identified several other aspects of tumor biology that could be manipulated in future treatments. These include interdicting tumor-stromal signaling processes that lead to the formation of stromal barriers around tumor cell clusters that might attenuate drug access and immune signaling, MYO10 mediated signaling and motility along FLPs, and forced mitochondria-nucleus proximity that might alter aspects of DNA damage repair and/or ROS signaling.

Overall, this multi-analyte, treatment-response Atlas derived for a single patient from the OHSU SMMART program shows both the promise and challenges of a personalized approach to metastatic cancer treatment. A truly personalized approach requires sufficiently advanced methods for collecting and analyzing both clinical and molecular data, coupled with the ability to interpret results in the context of longitudinal samples from the same patient. We have now shown that acquisition, management, analysis, and interpretation of biospecimen to identify and act on mechanisms of resistance in a time frame needed for patient management is feasible. We acknowledge that the analytical methods are currently too complex to be widely applied but could be dramatically simplified once the utility of each assay platform is established.

Frequent measures of tumor response from CT/PET imaging and blood profiling provided rapid and quantitative information about overall tumor response to treatment, as well as information about heterogeneity in responses between lesions. This level of detail enables rapid assessment of responses to specific drug combinations and provides information about the extent to which tumor control is maintained after dose reductions needed to mitigate toxicity

effects. Together, these capabilities provide rationale and feasibility for treatment programs in which established and experimental drug combinations are rapidly tested for efficacy and replaced by more effective drugs as needed. Implementation of such a program promises for patients to both increase the duration of tumor control and reduce toxicity produced by continued administration of ineffective drugs.

The major challenges to Personalized Cancer Treatment yet to be fully addressed are drug access and the lack of strategies to manage heterogeneous tumors. Rapid elucidation of evolving resistance mechanisms and new therapeutic vulnerabilities can indicate off label use of drugs and drug combinations. Such a regimen raises safety and cost issues. The remarkable intermetastatic heterogeneity that clearly exists could suggest combining increasing numbers of drugs, which may not be manageable because of unacceptable toxicity or because of the realities of drug access and cost. One possible approach to counter this diversity is by cycling between drug combinations that affect different subsets of the disease. A further challenge is that a biopsy of a single metastatic lesion only reports on that particular lesion and, due to the small size of the biopsy, may not fully capture intrametastatic heterogeneity. Further development of assays for tumor components present in peripheral blood that report on overall tumor composition and burden might be better guides to such treatments than tissue biopsies.

Although there are significant challenges that must be overcome in order for the full impact of personalized cancer treatment to be realized, the present study suggests that success will be possible through clinical implementation of analytical approaches that are now being developed throughout the HTAN and elsewhere.

Acknowledgments

Work at OHSU on this project was carried out with major support from the National Institutes of Health (NIH), National Cancer Institute (NCI) Human Tumor Atlas Network (HTAN) Research Center (U2C CA233280), and the Prospect Creek Foundation to the OHSU SMMART (Serial Measurement of Molecular and Architectural Responses to Therapy) Program. The program was initiated with support from a Stand Up to Cancer-American Association for Cancer Research Dream Team Translational Cancer Research Grant, SU2C-AACR-DT0409. Additional support came from the OHSU Brenden-Colson Center for Pancreatic Care, the NIH/NCI Cancer Target Discovery and Development (CTD²) (U01 CA217842), a NIH/NCI Cancer Systems Biology Consortium Center (U54 CA209988), NIH/NCI U01 CA224012 (to LMC), a SBIR (R44 CA224994) (to KC), the Damon Runyon Cancer Research Foundation (to XN) and the M. J. Murdock Charitable Trust. Sequencing and multiscale microscopy was supported by the Knight Cancer Institute Cancer Center Support Grant (5 P30 CA69533). Electron microscopy was performed at the Multiscale Microscopy Core, light microscopy was performed using equipment in the Advanced Light Microscopy Core, both OHSU University Shared Resource Cores. Short read sequencing assays were performed by the OHSU Massively Parallel Sequencing Shared Resource.

We thank the following teams for their assistance with this study:

Clinical: Raymond Bergan, Christopher Corless, Alexander R. Guimaraes, Ben Kong, Zahi Mitri, and George Thomas.

Research Operations: Heidi S. Feiler, Joe W. Gray, Brett E. Johnson, Jamie Keck, Taylor Kelley, Marlana Klinger, Annette Kolodzie, Gordon B. Mills, Max Morris, Anastasiya Olson, Swapnil Parmar, Kiara Siex, Jayne M. Stommel, and Leanna Williams.

Information management: Patrick Leyshock, Georgia Mayfield, Souraya Mitri, Damir Sudar, Matt Viehdorfer, and Christina Zheng.

Nucleic acids: Christopher Boniface and Paul T. Spellman.

Proteins: Aurora Blucher and Marilyne Labrie.

Omics analysis: Özgün Babur, Allison L. Creason, Emek Demir, Joseph Estabrook, Jeremy Goecks, Laura M. Heiser, Janice Patterson, and Julia Somers.

Image analysis: Erik Burlingame, Young Hwan Chang, and Guillaume Thibault.

mIHC: Teresa Beechwood, Konjit Betre, Courtney B. Betts, Gina Choe, Lisa M. Coussens, Giovanney Gonzalez, Nell Kirchberger, Lauren Maloney, and Shamilene Sivagnanam.

CyclF: Elmar Bucher, Koei Chin, and Jennifer Eng.

FIB-SEM: Dylan Blumberg, Cecilia Bueno, Kaylyn Devlin, Yingsi Gao, David Kilburn, Moqing Liu, Kevin Loftis, Jessica L. Riesterer, Hannah Smith, Rebecca Smith, Kevin Stoltz, and Erin S. Stempinski.

STORM: Xiaolin Nan and Jing Wang.

Author Contributions

Conceptualization, R.B., G.B.M., and J.W.G.; Methodology, B.E.J., J.K., S.P., A.K., K.C., X.N., L.M.H., P.T.S., E.D., L.M.C., C.C., J.G., and J.W.G.; Software, A.L.C., P.L., S.S., D.S., G.Thibault, E.D., and Y.H.C.; Formal Analysis, A.L.C., A.B., C.B., E.Bucher, E.Burlingame, J.E., M.L., J.P., S.S., and G.T.; Investigation, B.E.J., J.K., B.K., S.P., C.B.B., C.B., K.C., J.E., J.L.R., X.N., G.Thomas, A.R.G., and C.C.; Resources, R.B. and Z.M.; Data Curation, A.L.C., J.K., S.P., S.M., and C.Z.; Writing – Original Draft, B.E.J., A.L.C., J.M.S., J.K., S.P., C.B.B., K.C., J.L.R., J.G., and J.W.G. Writing – Review & Editing, B.E.J., A.L.C., J.M.S., J.K., C.B.B., A.B., K.C., A.K., B.K., M.L., J.L.R., L.M.C., J.G., R.B., Z.M., G.B.M., and J.W.G.; Visualization, A.L.C., J.M.S., S.P., C.B.B., E.Burlingame, K.C., J.E., M.L., J.P., J.L.R., and X.N.; Supervision, C.C., J.G., R.B., Z.M., G.B.M., and J.W.G.; Project Administration, B.E.J., S.P., H.S.F., and A.K.; Funding Acquisition, L.M.C., C.C., J.G., R.B., G.B.M., and J.W.G.

Declaration of Interests

DS is employed by Quantitative Imaging Systems, which sells image analysis software.

LMC is a paid consultant for Cell Signaling Technologies, Shasqi Inc., and AbbVie Inc.; received reagent and/or research support from Plexxikon Inc., Pharmacyclics, Inc., Acerta Pharma, LLC, Deciphera Pharmaceuticals, LLC, Genentech, Inc., Roche Glycart AG, Syndax Pharmaceuticals Inc., Innate Pharma, and NanoString Technologies; and is a member of the Scientific Advisory Boards of Syndax Pharmaceuticals, Carisma Therapeutics, Zymeworks, Inc, Verseau Therapeutics, Cytomix Therapeutics, Inc., and Kineta Inc.

RB is a co-owner of Third Coast Therapeutics, that has option to license patents he holds.

GBM has licensed technologies to Myriad Genetics and Nanostring; is on the SAB or is a consultant to Amphista, AstraZeneca, Chrysalis Biotechnology, GSK, ImmunoMET, Ionis, Lilly, PDX Pharmaceuticals, Signalchem Lifesciences, Symphogen, Tarveda, Turbine, and Zentalis Pharmaceuticals; and has stock/options/financial interests in Catena Pharmaceuticals, ImmunoMet, SignalChem, and Tarveda.

JWG has licensed technologies to Abbott Diagnostics; has ownership positions in Convergent Genomics, Health Technology Innovations, Zorro Bio and PDX Pharmaceuticals; serves as a paid consultant to New Leaf Ventures; has received research support from Thermo Fisher Scientific (formerly FEI), Zeiss, Miltenyi Biotech, Quantitative Imaging, Health Technology Innovations and Micron Technologies; and owns stock in Abbott Diagnostics, AbbVie, Alphabet, Amazon, Amgen, Apple, General Electric, Gilead, Intel, Microsoft, Nvidia, and Zimmer Biomet.

Figure Legends

Figure 1. Workflows and analytical platforms used in generation of the Atlas.

Figure 2. Timeline of treatment and response metrics.

(A) Treatment schedule and biopsy timing (red stars) over the course of three phases of treatment (red, blue, and green areas). The duration and relative dose for each drug is indicated by the extent and width of a horizontal bar. Continuation of a drug after the end of Phase 3 is indicated by a right pointing arrow. **(B)** Clinically reported serum levels of three tumor protein biomarkers. CEA values were multiplied by 5 to facilitate visualization. **(C)** Longitudinal tracking and variation in the longest-axis size of 15 representative metastatic lesions measured from serial CT images. The anatomic locations of the lesions are indicated in the figure. The results of FDG-PET imaging are indicated by circles, colored and centered on the lines of their corresponding lesion. The diameter of each circle is proportional to the background-normalized SUVmax. See also Figures S1, S2, and Table S1.

Figure 3. Genomic evolution and mechanisms of therapeutic response and resistance revealed by integrative omic analyses.

(A) Comparison of somatic genetic alterations. Single Nucleotide Variants and Insertion-Deletions were identified from whole exome sequencing (WES) of tissue samples and classified as Ubiquitous (present in all samples; blue), Shared (present in at least two samples; green), or Private (present in only a single sample; red). Variants detected in at least 2 reads but not independently called are shown with reduced opacity. **(B)** Phylogenetic tree showing the evolutionary relationship between the primary tumor and two metastases generated from somatic genetic alterations identified from WES data across all four tissue samples. A *CCND1* gain was ubiquitous, a pathogenic *PIK3CA* p.E542K mutation was private to Bx2, and a *TYMS* amplification was private to Bx3. **(C)** Transcriptomic gene set variation analysis (GSVA) of Cancer Hallmark pathways. The boxplot represents the distribution (upper and lower quartiles and median) of GSVA scores for the TCGA Luminal breast cancer cohort. Enrichment scores also are shown for patient samples Bx1 (green line), Bx2 (orange line), and Bx3 (purple line). **(D)** RPPA protein pathway activity assessment using pathway scores. The boxplot represents the distribution of the pathway activity of the TCGA breast cancer cohort as well as the pathway activities of patient samples Bx1 and Bx2. **(E)** Intracellular Signaling Protein Panel measurements of total and phosphoprotein levels in Bx2 and Bx3. The boxplots represent the distribution of protein levels of 57 metastatic breast cancers and compared to Bx2 and Bx3. **(F)** Total and phosphoprotein levels from RPPA analyses. Protein expression values were normalized within the TCGA breast cancer cohort. The heat map represents a rank sum ordering of protein expression based on the fold-change of Bx2 relative to Bx1 with selected proteins highlighted. **(G)** Phosphoproteins in the PI3K-AKT-mTOR pathway effected by everolimus in Bx2, as summarized from RPPA data. Everolimus leads to decreased phosphoprotein activity downstream of mTORC1, but multiple phosphoproteins are increased in the PI3K-AKT arm of the pathway, possibly through mutant PI3K E542K activity or feedback signaling to mTORC2. **(H)** Protein and phosphoproteins in cell cycle regulatory pathways effected by palbociclib, as summarized from RPPA data of Bx2. Palbociclib should activate RB1 by inhibiting its phosphorylation by the Cyclin D/CDK4/6 complex. However, Bx2 had continued high levels of RB1 phosphorylation and tumor cell proliferation on palbociclib, possibly due to RB1 inactivation by cyclin/CDK2 complexes that remain active due to PI3K-AKT-dependent degradation of the CDK2 inhibitor p21. Inferred activities or regulation in both (G) and (H) are based on total or phosphoprotein quantity combined with known function to reflect relative increases (red), decreases (pink, green), or unchanged/unknown (yellow) activities. See also Figure S3 and Table S2.

Figure 4. Monitoring response to therapy with deep *in situ* immune phenotyping by mIHC

(A) Primary tumor (PT) and three biopsies (Bx1-3) were subjected to multiplex immunohistochemical (mIHC) analyses quantitatively evaluating immune (CD45⁺) and epithelial (Pan cytokeratin/CK⁺) positive cells in tumor compartments enumerated as % of total nucleated cells, and by overall cell density (#cells/mm² tissue analyzed). **(B)** Graphical representation of tissue composition, showing proportion of PanCK⁺, CD45⁺, and PanCK⁻ CD45⁻ (other) nucleated cells. **(C)** Immune composition (as percent of total CD45⁺ cells) comparisons of seven major leukocyte lineages, including macrophages and monocytes (mac/mono). **(D)** Deeper auditing of leukocyte lineages in Bx1 and Bx2 enumerating 13 immune cell populations and functional states. **(E)** Total CD3⁺ T cell abundance (orange pie slice) of total CD45⁺ cell populations (left), and proportion of CD4⁺ (blue) and CD8⁺ T cells (gray) within total T cells (right) in the primary tumor and three biopsies. **(F)** Presence of PD-1⁺ cells (as percent of total CD3⁺ T cells) in both the CD3⁺CD4⁺ and CD3⁺CD8⁺ T cell populations. **(G)** Differentiation state of CD3⁺CD4⁺ T cells reflected by regulatory (Treg), Th1, Th2, Th17, and Th0/γδ subsets (left), and CD3⁺CD8⁺ T cells as reflected by expression of PD-1 and EOMES. **(H)** Differentiation state of CD3⁺CD4⁺ T cells reflected by regulatory (Treg), Th17, Th1, Th2, and Th0/γδ subsets in Bx1 and Bx2. See also Figure S4 and Table S2.

Figure 5. Monitoring tumor and stromal responses to therapy using CyclIF and FIB-SEM

(A) Z-score heatmap showing 11 subpopulation clusters (0-10), which were generated from unsupervised cluster analysis of 20 protein expression levels for all cells in Bx1, Bx2, Bx3, HER2 Luminal, normal breast, tonsil, and six cell lines (T47D, BT474, AU565, HCC3153, HCC1143, and MDA-MB-436). Cluster IDs and annotations are on the right. The color scale bar indicates log transformed protein expression after Z-score normalization. Abbreviations: Lum – Luminal, Bas – Basal, Mes – Mesenchymal. **(B)** Composite CyclIF high power images from Bx1 (left), Bx2 (middle), and Bx3 (right). The scale bars indicate 20 μm. Green, red, turquoise, and gray colors represent Vimentin (fibroblast), CD31 (endothelial), E-cadherin (epithelial), and DNA (nuclei), respectively. **(C)** Bar plots showing cell compositions in Bx1, Bx2, Bx3, and reference tissues (cell lines; T47D, BT474, HCC1143), normal breast (Norm Breast), and HER2+ Luminal B subtype breast cancer (HER2 Lum). Cluster compositions for all cell types are shown in the left panel, for epithelial cells in the center panel, and for non-epithelial in the right panel. **(D)** Histograms showing distances from tumor cells to the nearest immune cells (top two panels; macrophage and T cell) and to the nearest endothelial cells and fibroblasts (bottom two panels). **(E)** Two views of reconstructed 3D FIB-SEM data from Bx1 showing the intimate relationship between the cancer cells (red and pink) and the fibroblasts (blue and turquoise). The close-up view on the top shows nanoscale cell-cell interactions, while the pulled-out full volume view on the bottom shows the fibroblasts wrapping around the tumor nest creating a protective barrier. Scale bars = 5 μm. Movies showing these interactions in more detail are available as supplementary material. See also Figure S5 and Table S5.

Figure 6. Therapy related inter- and intracellular compositions and interactions revealed using focused ion beam-scanning electron microscopy (FIB-SEM).

(A) 3DEM side-view rendering of a cell from Bx2 showing the length of filopodia extensions, while also exhibiting alignment of the internal mitochondria. Scale = 3 μm. **(B, C)** Two different views of the same reconstructed 3DEM data from Bx2 showing the paddle-shaped lamellipodia of the green and purple cells and the long filopodia extending from the red (same cell as in **A**) and blue cells into the stroma and interacting with neighboring cells. The purple cell and red cell from **(A)** were removed from view in **(B)** and **(C)**, respectively, to more easily show the protrusions. Scale = 1 μm. **(D)** 3DEM view showing high mitochondrion density residing in nuclear folds in Bx2. Scale = 1 μm. **(E)** Large electron-dense lysosomal granules were identified

in Bx2 3DEM volume and found dispersed between macropinosomes. Scale = 1 μm . (F) Additional detail from Bx1 of the nuclear invaginations and organization of mitochondria and macropinosomes. Scale = 1 μm . (G) Qualitative summary of ultrastructural feature prevalence with respect to normal tissue. Panels A, D, F color key: blue = nucleus, magenta = mitochondria, orange = nucleoli, yellow = macropinosomes; Panel E color key: green = lysosomes, red = macropinosomes. See also Figure S6 and Movies S1-4.

Tables

None

Methods

Patient Consent and Biospecimen Collection

This study was approved by the Oregon Health & Science University (OHSU) Institutional Review Board (IRB). All biospecimens and data were acquired and analyzed under the OHSU IRB-approved protocols *Molecular Mechanisms of Tumor Evolution and Resistance to Therapy* (IRB#16113) and *Reconstructing the Tumor Genome in Peripheral Blood* (IRB#10163). Informed written consent was obtained from the subject.

Resource Availability

All primary datasets from clinical and exploratory analytics generated during this study are available through the HTAN Data Coordinating Center (<https://humantumoratlas.org/>) as patient HTA9_1 in the OMS Atlas.

The published article includes all clinical metadata analyzed during this study (Table S1).

This study did not generate new unique reagents.

Radiology

FDG-PET/CT imaging was performed according to the standard institutional protocol, with patients fasting for 6 hours following 24 hours of rest. Prior to the examination and FDG injection, blood glucose levels were confirmed to be less than 200 mg/dL. The patient received a dose of ^{18}F -FDG of 370 to 555 MBq (10-15 mCi) on the basis of body weight. After an uptake period of 90 minutes, a vertex-to-midthigh FDG-PET/CT scan was performed using 3 min/bed position on a CTI Biograph duo PET/CT scanner (Siemens Medical Systems, Hoffman Estates, Illinois, USA) or a CTI Biograph TruePoint 40 PET/CT scanner (Siemens Medical Systems, Knoxville, Tennessee, USA). CT imaging was performed according to the standard institutional protocol from clavicles to mid-thigh on a Phillips Brilliance CT 128slice helical scanner (Phillips Medical Systems, Amsterdam, NE).

Pre- and on-treatment FDG PET/CT studies were reviewed by an expert nuclear medicine physician with analysis performed by a body imager with 15 years of experience in oncologic imaging. Target lesions were selected by having maximum standard uptake values (SUVs) greater than normal mediastinum average (lymph nodes), and greater than background liver SUV (liver lesions) and were recorded on the pre- and on-treatment scans at the same tumor region. Image analysis was performed using syngo via advanced visualization software (Siemens Healthcare GmbH, Erlangen, Germany) and Horos visualization software (Horos, Lausanne, Switzerland). All lesions meeting these criteria were recorded both on FDG-PET/CT and combined with long axis measurements (e.g., liver, splenic, lung lesions) and long and short-axis measures (lymph nodes) at all time points during the care of the patient. All SUVmax measures were normalized by subtracting the mean background SUVmax from the organ of origin (e.g., mediastinum or liver).

GeneTrails[®] Solid Tumor Panel

The GeneTrails Solid Tumor Panel is performed by the OHSU Knight Diagnostic Laboratories on genomic DNA extracted from macro-dissected, tumor-rich regions of formalin-fixed paraffin-embedded tissue (FFPE). Next-generation sequencing libraries were prepared using custom QIASeq chemistry (QIAGEN) with multiplexed PCR, and sequenced on an Illumina NextSeq500/550. The DNA library was generated by 9,229 custom-designed primer extension assays covering 613,343 base pairs across 225 cancer-related genes (including whole exons of 199 genes and hotspot regions of 26 genes). This panel is routinely sequenced to an average read depth of >2,000, providing high sensitivity for SNVs, short insertions/deletions, and copy number alterations. Variants were identified using both FreeBayes and MuTect2 algorithms in a custom sequencing analysis pipeline.

Blood collection and DNA isolation for WES and DIDA-Seq

Up to 40 mL (range 6-40 mL) of blood were collected in 5x 6-mL or 4x 10-mL, purple-capped EDTA tubes. Consistent with published recommendations (Merker et al., 2018), blood plasma was isolated within 6 h of collection by first spinning whole blood at 1000g for 10 min, separating the top plasma layer into 1 mL aliquots, then spinning those aliquots at 15,000g for 10 min, transferring the supernatant to cryovials, and storing at -80°C. DNA extraction of tumor tissue from FFPE was carried out using QIAGEN FFPE DNA extraction kit (QIAGEN). DNA was extracted from plasma and buffy coat using Macherey-Nagel NucleoSnap and QIAGEN Blood and Tissue kits, respectively. DNA isolated from both FFPE samples and buffy coat were fragmented by sonication to 150 bp using a Covaris E220 prior to library preparation.

Whole Exome Sequencing (WES)

Sequencing libraries were prepared using 100-500 ng of cell free DNA (cfDNA) or sonicated genomic DNA using KAPA Hyper-Prep Kit (KAPA Biosystems) with Agilent SureSelect XT Target Enrichment System and Human All Exon V5 capture baits (Agilent Technologies). Next generation sequencing was carried out using the Illumina NextSeq500 or HiSeq 2500 platform with 2x79-144 cycles by the OHSU Massively Parallel Sequencing Shared Resource to an average depth of 100X per library replicate.

Somatic mutation calling: sequence read FastQ data files were aligned to the UCSC hg19 human genome build using BWA MEM (0.7.12, GATK, Broad Institute) (Li and Durbin, 2010) followed by marking duplicate reads (Mark Duplicates) and base recalibration (BQSR) (McKenna et al., 2010). Bam files for replicate libraries were merged and somatic variants were called using MuTect2 (4.0.4.0 GATK, Broad Institute) between tumor or cfDNA and the patient's matched normal from buffy coat (Cibulskis et al., 2013). A panel of normal (PON) and the gnomAD (release 2.0.1; <https://gnomad.broadinstitute.org/>) germline reference resource were used to filter out technical sequencing artifacts and common polymorphisms, respectively. All analysis tools were run using an OHSU Galaxy instance (v17.09) (Afgan et al., 2018).

Phylogenetic and Clonal Analysis: Mutect2 and mpileup (Li, 2011) were used to call or detect presence of variants across all samples. Only sequence reads with base quality greater than 20 and mapping quality greater than 30 were used for mpileup. Variants with VAF lower than 5% or depth lower than 30 reads were filtered. The R package ape (Paradis and Schliep, 2019) was used for phylogenetic analysis. A binary table of variants present across all tumor samples was generated as input. Genetic distance was estimated using the dist.gene function with the pairwise method. Minimum Evolution (ME) fit with ordinary least-squares (OLS) using the FastME function was used to reconstruct the phylogeny.

Copy Number Analysis: Copy number analysis was performed with CNVkit (v0.9.4a0) (Talevich et al., 2016) using the tumor/ctDNA aligned reads (BAM) and a pooled normal reference. On-

and off- target read depths from each sample were median-centered log₂ normalized, followed by GC bias correction and repeat masking. Tumor copy ratios were estimated by subtracting the log₂-normalized depths for each bin. Corrected copy ratio profiles were segmented using circular binary segmentation (CBS). Tumor purity estimates were then used to call each segment's absolute integer copy number.

Dual Index Degenerate Adaptor Sequencing (DIDA-Seq)

Bait Design: Single nucleotide variants (SNVs) were filtered by frequency (>5% in the tumor/cfDNA and <2% in the matched normal) and depth (>30x in the tumor/cfDNA and >15x in the matched normal). A set of 20-40 SNVs were then hand-curated and chosen per tumor tissue sample based on clonality and potential functional impact for bait design.

Library Preparation: We chose 53 mutations representative of all four classes of origin, both clonal and subclonal, functional and non-functional, to monitor longitudinal blood draws for the presence of tumor-derived circulating tumor DNA (ctDNA). DIDA-Seq error-correction libraries were created using the Kapa Biosystems Hyper Prep kit using at least 30 ng of cell-free DNA as input as previously described, using a single over-night capture incubation instead of two incubations (Butler et al., 2019). Samples were sequenced on either the Illumina HiSeq 2500, paired-end 100 bp, with dual 14-bp indexing cycles (highcapacity, rapid run mode) or the Illumina NextSeq 500, paired-end 75 bp with dual 14-bp indexing cycles (high-capacity, 150-cycle kit).

Error-Correction, Bait Evaluation, and Variant Analysis: The pipeline for analyzing DIDA-Seq data was based on the duplex sequencing pipeline developed in the Loeb laboratory at the University of Washington with substantial modification to be compatible with our data (Kennedy et al., 2014). The DIDA-Seq computational pipeline was implemented as previously described (Butler et al., 2019) and the variant allele frequency was determined for each mutation at each time point. Each panel of baits corresponding to variants found in a given tissue or set of tissues (primary, Bx1, and Bx2) was evaluated using unrelated patient cfDNA samples (negative controls). In our patient, we sequenced each library to an average post-error correction depth of 4,000-15,000X coverage per site-of-interest and determined the variant allele frequency (VAF). We compared the mutation-specific VAF in the patient's plasma to the VAF of the same site in the set of pooled negative controls (sequenced to an average post error-correction depth of 100,000X per site giving an average error rate of 1 in 30,000 reads). A p-value was generated for each site and sites aggregated by panel using the overlap coefficient of the beta distributions between the VAF in the sample and VAF in the negative controls (Montoya et al., 2019). Any site with greater than 1% VAF in the negative controls was omitted from further evaluation. Data points having a p-value greater than 0.05 were considered not statistically different from the negative controls, effectively determining our lower limit of detection given the individual or aggregated sites' sequencing depth at each time point.

RNA Sequencing and Transcriptomic Analysis

Library construction and sequencing: RNA was extracted from macro-dissected, tumor-rich regions of formalin-fixed paraffin-embedded tissue (FFPE) at the CLIA-certified/CAP-accredited OHSU Knight Diagnostics Laboratories. Sequencing libraries are constructed with the TruSeq RNA Exome Library Prep Kit followed by sequencing on Illumina NextSeq500. To allow for assessment and removal of technical artifacts (due to, e.g., library preparation), a Universal Human Reference (UHR) (Chem-Agilent, Catalog #740000) was sequenced with each batch of samples.

Gene Quantification: Transcript quantification followed the methods described by Tatlow and Piccolo (Tatlow and Piccolo, 2016). Briefly, the raw sequence reads were quality trimmed using Trim Galore (https://www.bioinformatics.babraham.ac.uk/projects/trim_galore/) followed by

pseudo-alignment and transcription quantification using Kallisto with GENCODE reference transcriptome (version 24). Transcript level expression is aggregated to gene level abundance using the R package tximport (Soneson et al., 2016) yielding expression values for 60554 Ensembl genes.

Batch Correction: Genes were filtered based on a minimum of 3 transcripts per million (TPM) in at least 3 of 48 samples, which included 29 ER+ metastatic breast cancer samples and 19 UHR samples. The filtered gene expression matrix (16,364 genes) was batch corrected by removing unwanted variation (RUV) (Peixoto et al., 2015; Risso et al., 2014). RUV correction uses factor analysis to identify the factors of unwanted variation observed in the UHR batch control and corrects for them across all samples. RUV was applied by removing 1 factor (k) using the 5% of genes with the lowest standard deviation. In addition to intra-cohort batch correct, the patient samples were batch adjusted for analyses comparing to the TCGA BRCA (Tatlow and Piccolo, 2016). The TCGA BRCA gene expression matrix was filtered to samples with a Luminal (A or B) molecular subtype and joined with the RUV corrected patient sample gene expression. The combined matrix was log transformed, filtered to genes with a minimum of 3 log₂ TPMs in at least 3 samples, and batched corrected using ComBat with TCGA samples set as the reference (Leek et al., 2012).

Molecular Subtype Signature: The PAM50 subtype gene signature was used to classify samples into the intrinsic molecular subtypes (Parker et al., 2009). A cohort of 20 ER+ and 20 ER- samples was used as the background for classifying the patient samples' subtypes. The gene expression matrix using these 40 samples and the patient samples was mean centered and correlated (Spearman) to the pre-defined centroids based from Parker et al. The samples were assigned to the molecular subtype with the highest Spearman correlation to the subtype centroid.

Pathway enrichment analysis: Gene set variation analysis (GSVA) was used to estimate pathway enrichment of the 1.) MSigDB Cancer Hallmark Pathways (50 gene sets), 2.) All MSigDB Pathways (~20K gene sets), and 3.) Reactome Pathway Database (~2K gene sets) (Hanzelmann et al., 2013); <https://bioconductor.org/packages/release/bioc/html/GSVA.html>; (Jassal et al., 2020; Liberzon et al., 2015). GSVA used a Gaussian kernel for estimating the cumulative density function and the enrichment statistic was calculated as the difference between the maximum positive/negative random walk deviations. This analysis was applied to the RUV/ComBat adjusted log₂ gene expression matrix that included both TCGA BRCA Luminal Samples and the patient samples.

Transcriptional regulator networks

Regulatory pathway and molecular interactions network: The regulatory network used to generate enrichment signatures is derived from the aggregation of publicly available molecular interactions and biological pathway databases provided by the Pathway Commons (PC) resource (Cerami et al., 2011). The aggregated data is represented in the standard Biological Pathway Exchange (BioPAX) language and provides the most complete and rich representation of the biological network models stored in PC. These complex biochemical reactions were reduced to pairwise relationships using rules to generate a Simple Interaction Format (SIF) representation of BioPAX interactions. The reduction of BioPAX interactions to the SIF allows for the representation of pairwise molecular interactions in the context of specific binary relationships. The feature space of the SIF regulatory network was restricted to primary and secondary downstream interactions for genes within Pathway Commons. The regulatory network was then reduced to edges that are associated with the binary relationship "controls-expression-of", defined as any reaction where the first protein controls a conversion or a template reaction that changes the expression of the second protein.

Network weight assignment: Weights are assigned to the protein-protein edges within the graph for each regulator-target pair within the regulatory network that is represented in the expression data set. These weights are derived from the integration of an F-test statistic to capture linear dependency and the Spearman rank-order correlation coefficient for a given regulator-target pair.

Regulon enrichment: This method leverages pathway information and gene expression data to produce regulon-based protein activity scores. Our method tests for positional shifts in experimental-evidence supported networks consisting of transcription factors and their downstream signaling pathways when projected onto a rank-sorted gene-expression signature. The gene-expression signature is derived by comparing all features to the median expression level of all samples considered within the data-set. After weights have been assigned to the regulatory network, the positive and negative edges of each regulator are rank ordered. The first component of the enrichment signature, the local delta concordance signature, is derived by capturing the concordance between the magnitude of the weight assigned to a particular edge and the ranked position of that edge. The features associated with activation, positive edges within the regulatory network, are monotonically ranked from most lowly to highly expressed in the restricted feature space, where the features that are repressed are ranked by a monotonically decreasing function. This component of the signature considers positive and negative edges independently, which captures support for an enrichment signature even if one of the edge groups is underrepresented in the network graph. The second component of the enrichment signature, the local enrichment signature, captures positional shifts in the local gene ranked signature and integrates those shifts with the weights assigned to overlapping features for a given regulon and the expression data set. The last component of the enrichment signature considers the entire feature space and projects the rank-sorted local signature onto this global ranked feature space. We derive our global enrichment signature from this projection for each regulator we consider. We use the median of robust quantile-transformed ranked positions as the enrichment scores for both the local enrichment and global enrichment signatures. We then integrate these three individual signatures together, which allows us to capture differences between individual regulator signatures within the context of an individual patient as well as at a cohort level.

Reverse Phase Protein Arrays

Protein extracts from tumor samples were analyzed as previously described (Labrie et al., 2019b; Tibes et al., 2006). In order to scale the protein expression values, the RPPA data from the patient samples was merged within the TCGA breast cancer RPPA dataset, using the replicate-based normalization method (Akbari et al., 2014). The protein expression values were then z-scored by using the median and standard deviation and a heat-map was generated from the treated and untreated samples, using Rank-Sum ordering of the proteins fold change. The heat map was produced using publicly available Cluster 3.0 and TreeView software.

Pathway Analysis: All pathway predictors have been previously described (Labrie et al., 2019b). Proteins used as predictors of the different pathways are listed in Table S2. To determine a pathway score, for each sample all positively associated predictors were summed minus the predictors that are negatively associated with the pathway. The total was then divided by the numbers of predictors in the pathway. To generate the pathway scores histograms, the distribution of each TCGA samples subtype was plotted and the value of the patient pre- and post-treatment sample was added to the histograms.

Intracellular Signaling Protein Panel

The Nanostring 3D Vantage Solid Tumor Panel is comprised of 27 antibodies, including 13 phosphorylated protein targets, specifically designed to interrogate the MAPK and PI3K/mTOR

signaling pathways (Lee et al., 2018). This multiplexed panel allows for the simultaneous quantification of multiple proteins from a single section of FFPE tissue. Four micron sections of FFPE cancer cell lines (controls) or tumor biopsy tissue were subjected to citrate-based antigen retrieval and incubated overnight with the cocktail of oligo-tagged antibodies. After washing, the oligo-tags were released by UV light (3 minutes on a UV lightbox) and quantified using the Nanostring nCounter system. A set of 6 FFPE cancer cell lines were selected as positive controls and included on every run to assess antibody and control performance and to correct for batch effects. Batch correction was performed using Removal of Unwanted Variation (RUV) using the replicate positive controls to estimate the factors associated with batch effect (Molania et al., 2019). RUV parameters were optimized by measuring the consistency of replicate controls and careful evaluation of outliers to ensure validity of results. This assay was validated for clinical use in the Knight Diagnostic Laboratories at OHSU as the GeneTrails® Intracellular Signaling Protein Panel.

Integrative Analyses

Multi-omic integrated pathway analysis: CausalPath (<https://github.com/PathwayAndDataAnalysis/causalpath>; [commit 9f8d6f8](#)) was used for integrated pathway analysis of protein, phosphoprotein, and gene abundance (<https://www.biorxiv.org/content/10.1101/258855v4>). Briefly, CausalPath is a hypothesis generating tool that uses literature-grounded interactions from Pathway Commons to produce a graphical representation of causal relationships that are consistent with patterns in a multi-omic datasets (Rodchenkov et al., 2020). This integrative approach allows for holistic evaluation of signaling networks and pathway activity across longitudinal biopsies. The CausalPath analysis used the log fold change of total and phosphoprotein (RPPA) and gene expression from Bx1 and Bx2 with the following parameters: threshold-for-data-significance = 0.4 for RNA, protein, and phosphoprotein, value-transformation = max, calculate-network-significance = true, permutations-for-significance = 10,000, color-saturation-value = 2.5, data-type-for-expressional-targets = rna and protein, show-all-genes-with-proteomic-data = true, and show-insignificant-data = true. The transcriptional regulon enrichment activity was mapped and overlaid on to the CausalPath generated network. The network was pruned to focus on the pathways related to the targets of the Phase I therapies.

Integrated Heatmap: The gene, protein, phosphoprotein abundances, and transcriptional regulon enrichment activities were integrated into a single heatmap. Each data type was independently scaled to -1 to 1 with the exception of protein/phosphoprotein, which were scaled together. Fold change of biopsy 2 to biopsy 1 was calculated for each scaled feature and represented as a heatmap grouped by pathway categories of interest.

Multiplex Immunohistochemistry

Immunohistochemical staining: Glass mounted FFPE tissue sections (5 µm) were baked at 60°C for 60 minutes, deparaffinized with xylene, and rehydrated in serially graded alcohols, then place in distilled water. Slides were stained with hematoxylin (Dako, S3301) for 1 minute, mounted with 1x TBST buffer (Boston Bioproducts, IBB-181R), coverslipped with Signature Series Cover Glass (Thermo Scientific, 12460S), and subjected to whole slide digital scanning at 20x magnification using an Aperio ImageScope (Leica Biosystems). Slides were de-coverslipped with 1 min of agitation in TBST, and subjected to heat-mediated antigen retrieval in 1x pH 6.0 citrate buffer (Biogenex Laboratories, HK0809K) for 20 min at 95°C followed by blocking of endogenous peroxidase activity (Dako, S2003, per manufacturer's instructions). Slides were then subjected to 12 cycles of multiplex immunohistochemistry (mIHC), each cycle consisted of either 1 or 2 rounds of IHC. Each round consisted of immunodetection (primary antibody, HRP-linked secondary antibody, HRP-mediated development of AEC chromogen),

and whole slide scanning. Citrate antigen retrieval was used between cycles to remove primary antibodies, and HRP inactivation was used between rounds (Dako, S2003, per manufacturer's instructions) to eliminate HRP carry-over as described previously (Banik et al., 2020; Tsujikawa et al., 2017). Several antibody panels (and variations of) were utilized for the current study (Table S2). Where IHC and chromogenic staining did not pass QC, they were not included in analysis: e.g., PD-L1 and CSF1R on the myeloid panel, and CD68 and ICOS on the functional panel(s). Several antibodies were not common across all or some panels, thus not included in results: IDO on functional panel (Bx1), Tryptase on myeloid panel (Primary, Bx1 and Bx2), RORyT and GATA3 on the lymphoid panel (primary, Bx1, and Bx2), and CCR2, HLA class-I, CD169, CD11b, and CD11c on the discovery panel (23 antibodies) (Bx3).

Image analysis pipeline: Regions of interest (ROIs) were selected from hematoxylin-stained images reflecting histopathologic regions containing either primary or metastatic tumor foci via analysis in ImageScope (Leica). Digitally-acquired images were registered in MatLab (MathWorks) utilizing the SURF algorithm in the Computer Vision Toolbox. Nuclear segmentation and color deconvolution were performed using an in-house FIJI macro (Image J, NIH) for segmenting hematoxylin only stained tissue. In short, preprocessing to isolate signal and remove background was performed, then nuclear objects were identified by watershed and standard image processing (erosion, dilation, and noise removal). AEC chromogenic signal was extracted by converting images from RGB to CMYK in ImageJ with the NIH plugin RGB_to_CMYK. The contrast of AEC chromogen intensities on a 0-255 scale in the yellow channel, as compared to RGB or the built-in AEC deconvolution vector, utilized the full intensity scale without a threshold. First, each channel was normalized by dividing all pixels in each image by the max intensity of that image to rescale image intensity values to a range 0 - 1. Next, rescaled isolated signal from each stain was quantified for every indexed nuclear object by a pipeline created in Cell Profiler 3.1.5 (Broad Institute). Image cytometry hierarchical gating was performed in FCS Express Image Cytometry RUO 6.1.4 (DeNovo Software) to quantify distinct populations of cells with spatial context.

Cyclic Immunofluorescence

Immunohistochemical analyses of tumor tissue: FFPE human tissues were sectioned at 4 μm and mounted on adhesive slides (Mercedes Medical, TNR WHT45AD). The slides were baked overnight in an oven at 55 $^{\circ}\text{C}$ (Robbin Scientific, Model 1000) and an additional 30 minutes at 65 $^{\circ}\text{C}$ (Clinical Scientific Equipment, NO. 100). Tissues were deparaffinized with xylene and rehydrated with graded ethanol baths. Two step antigen retrieval was performed in the Decloaking Chamber (Biocare Medical) using the following settings: set point 1 (SP1), 125 $^{\circ}\text{C}$, 30 seconds; SP2: 90 $^{\circ}\text{C}$, 30 seconds; SP limit: 10 $^{\circ}\text{C}$. Slides were further incubated in hot pH 9 buffer for 15 minutes. Slides were then washed in two brief changes of diH₂O (~2 seconds) and once for 5 minutes in 1x phosphate buffered saline (PBS), pH 7.4 (Fisher, BP39920). Sections were blocked in 10% normal goat serum (NGS, Vector S-1000), 1% bovine serum albumin (BSA, Sigma A7906) in PBS for 30 minutes at 20 $^{\circ}\text{C}$ in a humid chamber, followed by PBS washes. Primary antibodies (Table S2) were diluted in 5% NGS, 1% BSA in 1x PBS and applied overnight at 4 $^{\circ}\text{C}$ in a humid chamber, covered with plastic coverslips (IHC World, IW-2601). Following overnight incubation, tissues were washed 3 x 10 min in 1x PBS. Coverslips (Corning; 2980-243 or 2980-245) were mounted in Slowfade Gold plus DAPI mounting media (Life Technologies, S36938).

Fluorescence Microscopy: Fluorescently stained slides were scanned on the Zeiss AxioScan.Z1 (Zeiss, Germany) with a Colibri 7 light source (Zeiss). The filter cubes used for image collection were DAPI (Zeiss 96 HE), Alexa Fluor 488 (AF488, Zeiss 38 HE), AF555 (Zeiss 43 HE), AF647 (Zeiss 50), and AF750 (Chroma 49007 ET Cy7). The exposure time was determined individually for each slide and stain to ensure good dynamic range but not saturation. Full tissue scans were

taken with the 20x objective (Plan-Apochromat 0.8NA WD=0.55, Zeiss) and stitching was performed in Zen Blue image acquisition software (Zeiss).

Quenching Fluorescence Signal: After successful scanning, slides were soaked in 1x PBS for 10 – 30 minutes in a glass Coplin jar, waiting until the glass coverslip slid off without agitation. Quenching solution containing 20 mM sodium hydroxide (NaOH) and 3% hydrogen peroxide (H₂O₂) in 1x PBS was freshly prepared from stock solutions of 5 M NaOH and 30% H₂O₂, and each slide placed in 10 ml quenching solution. Slides were quenched under incandescent light, for 30 minutes for FFPE tissue slides. Slides were then removed from the chamber with forceps and washed 3 x 2 min in 1x PBS. The next round of primary antibodies was applied, diluted in blocking buffer as previously described, and imaging and quenching were repeated over ten rounds for FFPE tissue slides.

Cyclic IF quantification and analysis: Each image acquired during the Cyclic IF assay was registered based on DAPI features acquired from each round of staining (Young Hwan et al., 2017). Cellpose, a generalist algorithm for cellular segmentation (<https://www.biorxiv.org/content/10.1101/2020.02.02.931238v1>), was used to generate nuclear and cell segmentation masks with a pre-trained neural network classifier. Extracted single-cell features included centroids and mean intensity of each marker from its biologically-relevant segmentation mask (e.g., Ecad_Cytoplasm, Ki67_Nuclei). The last round DAPI image was used to filter out cells lost during each round of Cyclic IF staining.

For cell type determination and composition analysis, single cell mean intensities from each biopsy were log transformed and batch corrected using the scanpy regress_out function, which uses linear regression to remove batch variation (Wolf et al., 2018). Single cell mean intensities from positive control tissues and cell lines stained with biopsy two (Bx2) were log transformed and z-scored. The batch corrected biopsy values were divided by the ratio of each marker's mean intensity across all the positive control tissues to its mean intensity in Bx2, and all cells from the biopsy and control tissues were concatenated for clustering. Principal component analysis was performed with scanpy to reduce dimensionality, and unsupervised K-means clustering was performed on the principal components. The mean silhouette score of each value of k from 5 to 20 was calculated, and k=11 was selected for annotation, based on a relative maximum in mean silhouette score.

Scanning Electron Microscopy

Tissue for scanning electron microscopy (SEM) was collected at the time of biopsy and placed into SEM-specific fixative (2.5% paraformaldehyde, 2.5% glutaraldehyde in 0.1M sodium cacodylate buffer) as soon as possible for both pre-treatment and on-treatment biopsies. No tissue was collected for SEM from the third biopsy due to it originating from bone and decalcification protocols cannot yet reliably preserve ultrastructure for electron microscopy. Tissues were stored at 4°C in fixative and can remain that way nearly indefinitely.

Tissue samples were prepared for SEM by implementing a post-fixation heavy metal infiltration followed by epoxy-resin embedding (Epon 812). Heavy metal staining using osmium tetroxide, uranyl acetate, and lead aspartate provided contrast for imaging by dissociating the metals and allowing them to bind to lipids and proteins within cellular membranes and organelles. After staining and resin embedding, polymerized blocks were mounted directly to SEM pin-style stubs and trimmed to create a flat surface using a Leica UC7 ultramicrotome equipped with Diatome diamond knives. Mounted blocks were conductively coated with 8-nm carbon using a Leica ACE600 coater.

Two-dimensional large-format SEM maps were collected on trimmed block faces using a FEI Helios NanoLab G3 DualBeam™ focused ion beam-scanning electron microscope (FIB-SEM)

equipped with the Thermo Scientific Maps™ software package. Using this software for automation, hundreds of tiled images were collected over the entire block surface and stitched together, creating a pyramidal viewing architecture that provides observations starting at the millimeter-scale and zooms all the way down to 4-nm/pixel spatial resolution. Imaging conditions were 3 keV, 200-400 pA, 4-mm working distance, and 3 μ s dwell time using the concentric backscatter detector (CBS). A script developed in-house converts these large maps into ome.tiff format for web-based viewing.

Regions of interest for three-dimensional electron microscopy (3DEM) were selected from the high-resolution maps. Three separate 3DEM datasets collected using FIB-SEM technology were generated using vendor-specific automated serial-sectioning software: two high-resolution, small volumes (4-nm/voxel, 25 x 20 x 6-10 μ m³) on each respective biopsy and one lower resolution, larger volume (10-nm/voxel, 48 x 48 x 17 μ m³). The high-resolution image stacks were collected using the aforementioned Helios FIB-SEM with the same electron beam conditions and the In-Column Detector (ICD). The large volume was collected from the pre-treatment biopsy using a Zeiss Crossbeam 550 FIB-SEM using 1.5 keV, 1.0 nA, 5-mm working distance, 1.6 μ s dwell time, and the Energy-Selective Backscatter (EsB) detector. Segmentation of image stacks was performed manually in-house and by a CloudFactory managed workforce. Deep learning models developed in-house were utilized for nucleus and nucleoli segmentation on the high-resolution image stacks.

A more detailed description of the fixation procedure, sample preparation protocol, and imaging workflow can be found in a recently published open access book chapter (Riesterer et al., 2020) and via protocols.io:

“Sample fixation of biopsy tissue for Electron Microscopy (EM)”

dx.doi.org/10.17504/protocols.io.4bigske

“Post-Fixation Heavy Metal Staining and Resin Embedding for Electron Microscopy (EM)”

dx.doi.org/10.17504/protocols.io.36vgre6

“2D and 3D Electron Microscopy (EM) Imaging of Tissue Biopsies and Resections”

dx.doi.org/10.17504/protocols.io.bg58jy9w

All raw data, metadata, image stacks, and segmentation files are publicly available via the HTAN data portal and viewable via OMERO using the PathViewer plug-in.

Stochastic Optical Reconstruction Microscopy

SKBR3 cells (ATCC HTB0-30) were cultured in McCoy's 5A medium (Thermo Fisher Scientific 16600082) supplemented with 10% FBS (Thermo Fisher Scientific 10082147). For Stochastic Optical Reconstruction Microscopy (STORM) experiments, the cells were plated in LabTek chambered coverglass (Thermo Fisher Scientific 155409) for 36 to 48 hours before labeling and imaging. To prepare for imaging, the cells were first serum starved overnight (~16 hr); on the day of imaging, the cells were treated with 100 nM Alexa Fluor 647 conjugated trastuzumab for ~15 min, washed with pre-warmed blank medium, and placed on the microscope stage for imaging. Next, fresh STORM imaging buffer was added at 1:1,000 v/v dilution to the medium; the buffer is PBS supplemented with 0.5 mg/mL glucose oxidase (Sigma-Aldrich, G2133-50 kU), 40 μ g/mL catalase (Sigma-Aldrich, C100-50MG), and 10% D-Glucose (w/v, Fisher Chemicals D16-500); this was followed by addition of 10 mM (final concentration) mercaptoethylamine (MEA; Sigma-Aldrich, 30070). The sample was then explored at low 647 nm laser power (~100 W/cm²; this avoids unnecessary loss of AF647 due to photobleaching) to identify regions of interest. EGF (Cell Signaling 8916) was diluted from a 1 mg/mL stock in PBS to 10 mg/mL and then added to the cell culture at 1:100 v/v dilution to yield a final concentration of 10 ng/mL. Image acquisition was initiated right after adding EGF as described below.

Throughout the imaging process, the cells were kept in an on-stage incubator (TokaiHit) at 37°C with 5% CO₂.

The STORM microscope setup was the same as described previously (Creech et al., 2017). Briefly, a custom single-molecule fluorescence imaging setup was built on a Nikon Ti-U microscope frame, with other essential components including an objective lens with high numerical aperture (Nikon 60x oil, TIRF, NA = 1.49), a 647 nm laser (Coherent OBIS, max output = 140 mW; for exciting and converting AF647 into a dark state), a 405 nm laser (Coherent CUBE; for converting AF647 to fluorescent on-state), and an EM-CCD (Evolve 512 Delta, Photometrics), as well as other components including dichroic mirrors and emission filters. Image acquisition was performed using micromanager (Edelstein et al., 2010) with an EM-CCD gain setting typically set at 300 and the frame acquisition time 8 ms (possible by selecting a small region of interest). Typical power densities for the 647 nm and the 405 nm lasers were 1-2 kW/cm² and 1-20 W/cm², respectively. Raw STORM images were processed and reconstructed using custom Matlab scripts (Nickerson et al., 2015).

Alexa Fluor 647 conjugated trastuzumab was prepared using Alexa Fluor 647 NHS-ester (Thermo Fisher Scientific A37566) and purified according to manufacturer recommended procedures; the final dye to antibody conjugation ratio was measured to be around 2:1 using a UV-Vis spectrometer.

Supplemental Information

Figure S1. Related to Figure 2

A) Maximum intensity projection (MIP) FDG-PET from the beginning of Phase 1 treatment demonstrates multifocal FDG avid disease throughout the mediastinum, liver, spleen and skeleton, including target of Bx1 (arrow). **B)** Axial FDG-PET (from same timepoint as **A**) superimposed on CT showing FDG avid segment 6 liver lesion targeted by Bx1. **C)** Ultrasound image from Bx1. **D)** Axial contrast enhanced CT taken just before Bx2 demonstrates interval growth of a separate segment 5,6 liver lesion subsequently targeted by Bx2. **E)** Ultrasound image from Bx2. **F)** FDG-PET MIP image from the beginning of Phase 3 demonstrates a decrease in FDG avid lesions. Bx2 targeted lesion indicated (arrow). **G)** FDG-PET taken in Phase 3 one month before Bx3 demonstrates new FDG avid lesions in the L4 vertebral body, including the Bx3 targeted lesion (arrow). **H)** Axial FDG-PET (from same timepoint as **G**) superimposed on attenuation correction CT showing FDG avid segment targeted by Bx3. **I)** CT image from Bx3 demonstrates successful biopsy of the FDG avid, lytic lesion within the L4 vertebral body. Note the patient is prone during the biopsy. **J)** FDG-PET from the end of Phase 3 demonstrates continued response in most organs but a possible new progressing lesion within the liver (arrow). **K)** Axial FDG-PET (from same timepoint as **J**) superimposed on CT showing FDG avid possible liver lesion (arrow). **L)** Axial contrast enhanced CT taken during month 37 demonstrates nodular, heterogeneous, morphology of the liver showing signs of pseudocirrhosis (arrow).

Figure S2. Related to Figure 2

(A) Treatment schedule and biopsy timing (red stars) over the course of three phases of treatment (red, blue, and green areas). Individual drug's duration of treatment (bar width proportional to dose) and continuation after the end of Phase 3 (right pointing arrow), as indicated. **(B)** Clinically reported Absolute Neutrophil Count (ANC) in thousands per cubic millimeter (K/cu mm). **(C)** Clinically reported Platelet Count in thousands per cubic millimeter (K/cu mm). **(D)** Clinically reported results of liver function tests, including alkaline phosphatase (ALP), alanine aminotransferase (ALT), and aspartate aminotransferase (AST). **(E)** Longitudinal tracking of the average circulating tumor DNA (ctDNA) Variant Allele Frequency (VAF) of four

different groups of mutations: Variants private to Bx1 (Bx1), private to Bx2 (Bx2), shared between the primary, Bx1, and Bx2 (Bx1_Bx2_Primary), and shared by Bx1 and Bx2 but not the primary (Bx1_Bx2). Red boxed inset shows expanded ctDNA VAF timeline during a course of palliative radiotherapy during months 10-12. Red asterisks indicate dates of individual radiation fractions given.

Figure S3. Related to Figure 3

A) Single Nucleotide Variants and Insertion-Deletions were identified from whole exome sequencing of tissue samples and circulating tumor DNA from peripheral blood and classified as Ubiquitous (blue), Shared (green), or Private (red) (variants private to ctDNA timepoints not shown). Variants detected in at least 2 reads but not independently called are shown with reduced opacity. **B)** Comparison of copy number profiles. Scatter plots of copy number profiles from all four tissue samples: Primary (pink), Biopsy 1 (green), Biopsy 2 (orange), and Biopsy 3 (purple). **C)** Molecular Subtype. Bar plots show the Pearson correlation of the Primary (pink), Bx1 (green), Bx2 (orange), and Bx3 (purple) samples to the PAM50 subtype centroids. **D)** Integrated multi-omic pathway analysis. Pathway diagrams represent the integration of protein abundance (rectangles), phosphoprotein abundance (circle labeled 'P'; green outline indicates activating; red outline indicates inactivating), gene expression (circle labeled 'E'), and transcriptional regulator activity (circle labeled 'R'), and show the change in Bx2 relative to Bx1. The red and blue fill represent higher and lower expression/activity, respectively. **E)** Integrated multi-omic comparisons. The heatmap represents the change in Bx2 relative to Bx1 scaled (-1,1) expression/activity, with red representing an increase and blue representing a decrease in expression/activity, respectively. Grey indicates a gene or protein that is not measured by the assay or analysis. The row annotation bar indicates the pathway to which the genes/proteins belong.

Figure S4. Related to Figure 4

Hierarchical gating via image cytometry for identification of cell types and functional states elaborated by mIHC for: **(A)** myeloid, **(B)** lymphoid, **(C)** functional, and **(D)** discovery panel of antibodies.

Figure S5. Related to Figure 5

(A) Left panel: Clusters' composition bar plots of all cells in Bx1, Bx2, and Bx3, as well as reference tissues that were stained and processed with the Bx2 tumor. The 11 clustered cell subpopulations (0-10, left) based on unsupervised clustering analysis of CyclF image data (indicated by colors for tissue origins) are displayed. The cluster identities, matched to Figure 5A, are as follows: 0: Basal Ki-67 -- cells expressing basal cytokeratin (CK5, CK14, and CK17). 1: Mesenchymal Ki-67 -- cells expressing Vimentin, CD44 with Ki-67 and/or PCNA; 2: Lum/Basal: cells expressing both luminal cytokeratins (CK7 and CK19) and basal cytokeratins (CK5, CK14, and CK17), but not proliferation markers (Ki-67 and PCNA). 3: Immune (lymphoid) -- cells expressing one or more of CD45, CD3, CD4, and CD8. 4: Immune (myeloid) -- cells expressing CD68. 5: HER2 -- this cluster is only composed of HER2 positive cells that are mostly found in HER2 luminal, BT474, and AU55 cell lines but not in Bx1/Bx2/Bx3 tissues. 6: Lum ER^{hi} -- cells expressing luminal cytokeratins (CK7 and CK19) and high levels of ER. 7: Endothelial/Fibroblast -- two types of cells were lumped in this cluster. Cells expressing CD31 represent blood vessels. Cells expressing Vimentin or alpha smooth muscle actin represent mainly stromal fibroblasts, which are often present near CD31 positive endothelial cells. 8: Basal -- cells expressing basal cytokeratins (CK5, CK14, and CK19). 9: Lum ER^{med} Ki-67 -- cells expressing luminal cytokeratins (CK7 and CK19), E-cadherin, and intermediate level ER and Ki-67 or PCNA. 10: Lum ER^{hi} PCNA -- cells expressing luminal cytokeratins (CK7 and CK19) and high-level ER and PCNA. **Right panel:** Combined fraction and stacked bar plots of Bx1, Bx2,

and Bx3 tumors in each cluster. **(B)** The panels show alternative composite views of Figure 5B with ER (green), Ki-67 (red), CK19 (turquoise), and nuclei (gray) in the same regions of interest in each tumor with low (top panels) and high (bottom panels) magnifications. The scale bars indicate 50 μm and 20 μm , respectively, in low and high-power views. **(C)** Left panel: Cell type composition bar plot of all cells as described in (A). The cells in tumor, immune, and stroma are indicated by colors of cyan, green, and magenta, respectively. Right panel: Calculated Shannon Index (entropy) in each tissue is shown, representing the rate of heterogeneity based on the cell types defined in CyclIF image analysis. The index was obtained from single cell-based spatial analysis by counting cells and attributing cell type within 75 μm radius area from each cell. The order of tissues is coordinated in the two panels. **(D)** The results of further independent clustering for epithelial cells (left: clusters 0,1,2,5,6,8,9,10) and non-epithelial cells (right: clusters 3,4,7), i.e., supervised clustering analysis, are shown in two heatmaps (Z-Score) and composition changes of clustered subpopulations in Bx1, Bx2, and Bx3 are displayed under the corresponding heatmap.

Figure S6. Related to Figure 6

(A) The top-down, high-resolution blockface maps collected via SEM from Bx1 and Bx2 in the left column showing heterogeneity both intra-tumor and translationally. Bx1 shows well-defined nests of tumor cells separated by thick bands of collagen, while Bx2 shows nests, but the tissue is denser and collagen band thickness is reduced. The boxes marked on the maps measure 25 μm in the long direction and indicate where 3D FIB-SEM was collected. The right column shows the respective first slice from the 3D FIB-SEM volumes. Ultrastructural features of interest are marked as the following: (IN) invaginated nuclei, (FN) fenestrated nucleoli, (M) mitochondria, (L) lysosome, (S) stroma, (F) filopodia, (La) lamellipodia, and (MP) macropinosomes. **(B)** Filopodia-like protrusions (FLPs) direct EGF-induced cell movement of SKBR3 cells. Time-lapse stochastic optical reconstruction microscopy (STORM) images of SKBR3 cells labeled with Alexa Fluor 647-conjugated Herceptin, showing abundant FLPs decorated by HER2. Left image shows initial positions of the FLPs upon addition of EGF (10 ng/mL at around -30 s). Right image shows the same field of view after 1:30 min (90 s). The cyan crosses (1, 2, and 3) mark the original locations of the tips of corresponding FLPs. Scale bars, 1 mm.

Table S1. Related to Figure 2

Clinical metadata. Includes dates of all individual drug doses, results of serum tumor protein biomarker assays, neutrophil and platelet counts, liver function tests, CT and FDG-PET lesion measurements, and clinically reported immunohistochemical (IHC) assay results.

Table S2. Related to Figures 3-5

Exploratory analytic information. Includes gene set variation analysis scores of Reactome and MSigDB databases (RNAseq), transcriptional regulator activity scores (RNAseq), pathway signature analysis scores (RPPA), antibody panels used (mlHC and CyclIF), and classification of immune cell types by marker expression (mlHC).

Movie S1. Related to Figure 6

The 3D FIB-SEM volume collected at 4 nm/voxel resolution from Bx1 showing ultrastructural features at the nanoscale. Individual cell contours are rendered and illustrate the cell-cell and cell-stromal interactions. Aberrant nuclear morphology, clustered macropinosomes, organized mitochondria, and the presence of lysosomes are all observed in the 25 x 20 x 6 μm^3 volume.

Movie S2. Related to Figure 6

The 3D FIB-SEM volume collected at 4 nm/voxel resolution from Bx2 shows ultrastructural features at the nanoscale in a 25 x 20 x 10 μm^3 volume. Similar to the Bx1 volume, aberrant

nuclear morphology, clustered macropinosomes, organized mitochondria, and the presence of lysosomes are all observed. However, the cell-cell interactions are remarkable. The center tumor cell squeezing between the surrounding cells is observed to have micron-long protrusions, while its neighbors have clear lamellipodia.

Movie S3. Related to Figure 6

A larger 3D FIB-SEM volume ($60 \times 40 \times 18 \mu\text{m}^3$) collected at 10 nm/voxel resolution of Bx1 shows tumor nest interaction with the fibroblasts in the stroma. The fibroblasts in blue are interacting with the red cancer cells and wrapping themselves around the nest to form a barrier. In this case, the fibroblasts closest to the nest are observed to be blebbing.

Movie S4. Related to Figure 6

Live cell stochastic optical reconstruction microscopy (STORM) imaging of HER2 in a SKBR3 (HER2+ breast cancer) cell immediately after EGF treatment (at 10 ng/mL), highlighting the dynamics of HER2-enriched FLPs during a ~4 minute period. Note that the tips of most FLPs remained at their original locations and the cell body extended significantly in the form of lamellipodia toward the tips of the FLPs.

References

- Adurthi, S., Kumar, M.M., Vinodkumar, H.S., Mukherjee, G., Krishnamurthy, H., Acharya, K.K., Bafna, U.D., Uma, D.K., Abhishekh, B., Krishna, S., *et al.* (2017). Oestrogen Receptor-alpha binds the FOXP3 promoter and modulates regulatory T-cell function in human cervical cancer. *Sci Rep* 7, 17289.
- Afgan, E., Baker, D., Batut, B., van den Beek, M., Bouvier, D., Cech, M., Chilton, J., Clements, D., Coraor, N., Gruning, B.A., *et al.* (2018). The Galaxy platform for accessible, reproducible and collaborative biomedical analyses: 2018 update. *Nucleic Acids Res* 46, W537-W544.
- Akbani, R., Ng, P.K., Werner, H.M., Shahmoradgoli, M., Zhang, F., Ju, Z., Liu, W., Yang, J.Y., Yoshihara, K., Li, J., *et al.* (2014). A pan-cancer proteomic perspective on The Cancer Genome Atlas. *Nat Commun* 5, 3887.
- Allan, C., Burel, J.M., Moore, J., Blackburn, C., Linkert, M., Loynton, S., Macdonald, D., Moore, W.J., Neves, C., Patterson, A., *et al.* (2012). OMEERO: flexible, model-driven data management for experimental biology. *Nat Methods* 9, 245-253.
- Banik, G., Betts, C.B., Liudahl, S.M., Sivagnanam, S., Kawashima, R., Cotechini, T., Larson, W., Goecks, J., Pai, S.I., Clayburgh, D.R., *et al.* (2020). High-dimensional multiplexed immunohistochemical characterization of immune contexture in human cancers. *Methods Enzymol* 635, 1-20.
- Barros, M.H., Hauck, F., Dreyer, J.H., Kempkes, B., and Niedobitek, G. (2013). Macrophage polarisation: an immunohistochemical approach for identifying M1 and M2 macrophages. *PLoS One* 8, e80908.
- Buechler, C., Ritter, M., Orso, E., Langmann, T., Klucken, J., and Schmitz, G. (2000). Regulation of scavenger receptor CD163 expression in human monocytes and macrophages by pro- and antiinflammatory stimuli. *J Leukoc Biol* 67, 97-103.
- Butler, T.M., Boniface, C.T., Johnson-Camacho, K., Tabatabaei, S., Melendez, D., Kelley, T., Gray, J., Corless, C.L., and Spellman, P.T. (2019). Circulating tumor DNA dynamics using patient-customized assays are associated with outcome in neoadjuvantly treated breast cancer. *Cold Spring Harb Mol Case Stud* 5.

Cancer Genome Atlas, N. (2012). Comprehensive molecular portraits of human breast tumours. *Nature* **490**, 61-70.

Cerami, E.G., Gross, B.E., Demir, E., Rodchenkov, I., Babur, O., Anwar, N., Schultz, N., Bader, G.D., and Sander, C. (2011). Pathway Commons, a web resource for biological pathway data. *Nucleic Acids Res* **39**, D685-690.

Chen, M.M., Li, J., Wang, Y., Akbani, R., Lu, Y., Mills, G.B., and Liang, H. (2019). TCPA v3.0: An Integrative Platform to Explore the Pan-Cancer Analysis of Functional Proteomic Data. *Mol Cell Proteomics* **18**, S15-S25.

Cibulskis, K., Lawrence, M.S., Carter, S.L., Sivachenko, A., Jaffe, D., Sougnez, C., Gabriel, S., Meyerson, M., Lander, E.S., and Getz, G. (2013). Sensitive detection of somatic point mutations in impure and heterogeneous cancer samples. *Nat Biotechnol* **31**, 213-219.

Commisso, C., Davidson, S.M., Soydaner-Azeloglu, R.G., Parker, S.J., Kamphorst, J.J., Hackett, S., Grabocka, E., Nofal, M., Drebin, J.A., Thompson, C.B., *et al.* (2013). Macropinocytosis of protein is an amino acid supply route in Ras-transformed cells. *Nature* **497**, 633-637.

Creech, M.K., Wang, J., Nan, X., and Gibbs, S.L. (2017). Superresolution Imaging of Clinical Formalin Fixed Paraffin Embedded Breast Cancer with Single Molecule Localization Microscopy. *Sci Rep* **7**, 40766.

Desir, S., O'Hare, P., Vogel, R.I., Sperduto, W., Sarkari, A., Dickson, E.L., Wong, P., Nelson, A.C., Fong, Y., Steer, C.J., *et al.* (2018). Chemotherapy-Induced Tunneling Nanotubes Mediate Intercellular Drug Efflux in Pancreatic Cancer. *Sci Rep* **8**, 9484.

Edelstein, A., Amodaj, N., Hoover, K., Vale, R., and Stuurman, N. (2010). Computer control of microscopes using microManager. *Curr Protoc Mol Biol Chapter 14*, Unit14 20.

Eng, J., Thibault, G., Luoh, S.W., Gray, J.W., Chang, Y.H., and Chin, K. (2020). Cyclic Multiplexed-Immunofluorescence (cmIF), a Highly Multiplexed Method for Single-Cell Analysis. *Methods Mol Biol* **2055**, 521-562.

Ethier, J.L., Desautels, D., Templeton, A., Shah, P.S., and Amir, E. (2017). Prognostic role of neutrophil-to-lymphocyte ratio in breast cancer: a systematic review and meta-analysis. *Breast Cancer Res* **19**, 2.

Fassl, A., Brain, C., Abu-Remaileh, M., Stukan, I., Butter, D., Stepien, P., Feit, A.S., Bergholz, J., Michowski, W., Otto, T., *et al.* (2020). Increased lysosomal biomass is responsible for the resistance of triple-negative breast cancers to CDK4/6 inhibition. *Sci Adv* **6**, eabb2210.

Hafner, M., Mills, C.E., Subramanian, K., Chen, C., Chung, M., Boswell, S.A., Everley, R.A., Liu, C., Walmsley, C.S., Juric, D., *et al.* (2019). Multiomics Profiling Establishes the Polypharmacology of FDA-Approved CDK4/6 Inhibitors and the Potential for Differential Clinical Activity. *Cell Chem Biol* **26**, 1067-1080 e1068.

Hanahan, D., and Coussens, L.M. (2012). Accessories to the crime: functions of cells recruited to the tumor microenvironment. *Cancer Cell* **21**, 309-322.

Hanzelmann, S., Castelo, R., and Guinney, J. (2013). GSVA: gene set variation analysis for microarray and RNA-seq data. *BMC Bioinformatics* **14**, 7.

Herrera-Abreu, M.T., Palafox, M., Asghar, U., Rivas, M.A., Cutts, R.J., Garcia-Murillas, I., Pearson, A., Guzman, M., Rodriguez, O., Grueso, J., *et al.* (2016). Early Adaptation and Acquired Resistance to CDK4/6 Inhibition in Estrogen Receptor-Positive Breast Cancer. *Cancer Res* **76**, 2301-2313.

- Hosios, A.M., Hecht, V.C., Danai, L.V., Johnson, M.O., Rathmell, J.C., Steinhauser, M.L., Manalis, S.R., and Vander Heiden, M.G. (2016). Amino Acids Rather than Glucose Account for the Majority of Cell Mass in Proliferating Mammalian Cells. *Dev Cell* 36, 540-549.
- Iida, M., Nakamura, M., Tokuda, E., Toyosawa, D., Niwa, T., Ohuchi, N., Ishida, T., and Hayashi, S.I. (2019). The p21 levels have the potential to be a monitoring marker for ribociclib in breast cancer. *Oncotarget* 10, 4907-4918.
- Jassal, B., Matthews, L., Viteri, G., Gong, C., Lorente, P., Fabregat, A., Sidiropoulos, K., Cook, J., Gillespie, M., Haw, R., *et al.* (2020). The reactome pathway knowledgebase. *Nucleic Acids Res* 48, D498-D503.
- Kang, S., Bader, A.G., and Vogt, P.K. (2005). Phosphatidylinositol 3-kinase mutations identified in human cancer are oncogenic. *Proc Natl Acad Sci U S A* 102, 802-807.
- Kennedy, S.R., Schmitt, M.W., Fox, E.J., Kohn, B.F., Salk, J.J., Ahn, E.H., Prindle, M.J., Kuong, K.J., Shen, J.C., Risques, R.A., *et al.* (2014). Detecting ultralow-frequency mutations by Duplex Sequencing. *Nat Protoc* 9, 2586-2606.
- Kerber, M.L., and Cheney, R.E. (2011). Myosin-X: a MyTH-FERM myosin at the tips of filopodia. *J Cell Sci* 124, 3733-3741.
- Kim, J., and Guan, K.L. (2019). mTOR as a central hub of nutrient signalling and cell growth. *Nat Cell Biol* 21, 63-71.
- Knochelmann, H.M., Dwyer, C.J., Bailey, S.R., Amaya, S.M., Elston, D.M., Mazza-McCrann, J.M., and Paulos, C.M. (2018). When worlds collide: Th17 and Treg cells in cancer and autoimmunity. *Cell Mol Immunol* 15, 458-469.
- Labrie, M., Fang, Y., Kendsersky, N.D., Li, J., Liang, H., Westin, S.N., Mitri, Z., and Mills, G.B. (2019a). Using Reverse Phase Protein Array (RPPA) to Identify and Target Adaptive Resistance. *Adv Exp Med Biol* 1188, 251-266.
- Labrie, M., Kim, T.B., Ju, Z., Lee, S., Zhao, W., Fang, Y., Lu, Y., Chen, K., Ramirez, P., Frumovitz, M., *et al.* (2019b). Adaptive responses in a PARP inhibitor window of opportunity trial illustrate limited functional interlesional heterogeneity and potential combination therapy options. *Oncotarget* 10, 3533-3546.
- Lee, J., Geiss, G.K., Demirkan, G., Vellano, C.P., Filanoski, B., Lu, Y., Ju, Z., Yu, S., Guo, H., Bogatzki, L.Y., *et al.* (2018). Implementation of a Multiplex and Quantitative Proteomics Platform for Assessing Protein Lysates Using DNA-Barcoded Antibodies. *Mol Cell Proteomics* 17, 1245-1258.
- Leek, J.T., Johnson, W.E., Parker, H.S., Jaffe, A.E., and Storey, J.D. (2012). The sva package for removing batch effects and other unwanted variation in high-throughput experiments. *Bioinformatics* 28, 882-883.
- Li, H. (2011). A statistical framework for SNP calling, mutation discovery, association mapping and population genetical parameter estimation from sequencing data. *Bioinformatics* 27, 2987-2993.
- Li, H., and Durbin, R. (2010). Fast and accurate long-read alignment with Burrows-Wheeler transform. *Bioinformatics* 26, 589-595.
- Li, R., Waga, S., Hannon, G.J., Beach, D., and Stillman, B. (1994). Differential effects by the p21 CDK inhibitor on PCNA-dependent DNA replication and repair. *Nature* 371, 534-537.

- Liberzon, A., Birger, C., Thorvaldsdottir, H., Ghandi, M., Mesirov, J.P., and Tamayo, P. (2015). The Molecular Signatures Database (MSigDB) hallmark gene set collection. *Cell Syst* 1, 417-425.
- Lin, J.R., Fallahi-Sichani, M., and Sorger, P.K. (2015). Highly multiplexed imaging of single cells using a high-throughput cyclic immunofluorescence method. *Nat Commun* 6, 8390.
- Liu, Y., Dong, Y., Kong, L., Shi, F., Zhu, H., and Yu, J. (2018). Abscopal effect of radiotherapy combined with immune checkpoint inhibitors. *J Hematol Oncol* 11, 104.
- Llanos, S., Megias, D., Blanco-Aparicio, C., Hernandez-Encinas, E., Rovira, M., Pietrocola, F., and Serrano, M. (2019). Lysosomal trapping of palbociclib and its functional implications. *Oncogene* 38, 3886-3902.
- Marangoni, E., Laurent, C., Coussy, F., El-Botty, R., Chateau-Joubert, S., Servely, J.L., de Plater, L., Assayag, F., Dahmani, A., Montaudon, E., *et al.* (2018). Capecitabine Efficacy Is Correlated with TYMP and RB1 Expression in PDX Established from Triple-Negative Breast Cancers. *Clin Cancer Res* 24, 2605-2615.
- Massarweh, S., Romond, E., Black, E.P., Van Meter, E., Shelton, B., Kadamyian-Melkumian, V., Stevens, M., and Elledge, R. (2014). A phase II study of combined fulvestrant and everolimus in patients with metastatic estrogen receptor (ER)-positive breast cancer after aromatase inhibitor (AI) failure. *Breast Cancer Res Treat* 143, 325-332.
- McKenna, A., Hanna, M., Banks, E., Sivachenko, A., Cibulskis, K., Kernytsky, A., Garimella, K., Altshuler, D., Gabriel, S., Daly, M., *et al.* (2010). The Genome Analysis Toolkit: a MapReduce framework for analyzing next-generation DNA sequencing data. *Genome Res* 20, 1297-1303.
- Merker, J.D., Oxnard, G.R., Compton, C., Diehn, M., Hurley, P., Lazar, A.J., Lindeman, N., Lockwood, C.M., Rai, A.J., Schilsky, R.L., *et al.* (2018). Circulating Tumor DNA Analysis in Patients With Cancer: American Society of Clinical Oncology and College of American Pathologists Joint Review. *J Clin Oncol* 36, 1631-1641.
- Mi, W., Ye, Q., Liu, S., and She, Q.B. (2015). AKT inhibition overcomes rapamycin resistance by enhancing the repressive function of PRAS40 on mTORC1/4E-BP1 axis. *Oncotarget* 6, 13962-13977.
- Mitri, Z.I., Parmar, S., Johnson, B., Kolodzie, A., Keck, J.M., Morris, M., Guimaraes, A.R., Beckett, B.R., Borate, U., Lopez, C.D., *et al.* (2018). Implementing a comprehensive translational oncology platform: from molecular testing to actionability. *J Transl Med* 16, 358.
- Molania, R., Gagnon-Bartsch, J.A., Dobrovic, A., and Speed, T.P. (2019). A new normalization for Nanostring nCounter gene expression data. *Nucleic Acids Res* 47, 6073-6083.
- Montoya, J.A., Figueroa, G.P., and González-Sánchez, D. (2019). Statistical inference for the Weitzman overlapping coefficient in a family of distributions. *Applied Mathematical Modelling* 71, 558-568.
- Need, E.F., Selth, L.A., Harris, T.J., Birrell, S.N., Tilley, W.D., and Buchanan, G. (2012). Research resource: interplay between the genomic and transcriptional networks of androgen receptor and estrogen receptor alpha in luminal breast cancer cells. *Mol Endocrinol* 26, 1941-1952.
- Nelson, E.K., Piehler, B., Eckels, J., Rauch, A., Bellew, M., Hussey, P., Ramsay, S., Nathe, C., Lum, K., Krouse, K., *et al.* (2011). LabKey Server: an open source platform for scientific data integration, analysis and collaboration. *BMC Bioinformatics* 12, 71.

Nickerson, A., Huang, T., Lin, L.J., and Nan, X. (2015). Photoactivated Localization Microscopy with Bimolecular Fluorescence Complementation (BiFC-PALM). *J Vis Exp*, e53154.

O'Reilly, K.E., Rojo, F., She, Q.B., Solit, D., Mills, G.B., Smith, D., Lane, H., Hofmann, F., Hicklin, D.J., Ludwig, D.L., *et al.* (2006). mTOR inhibition induces upstream receptor tyrosine kinase signaling and activates Akt. *Cancer Res* 66, 1500-1508.

Ogawa, L.M., and Baserga, S.J. (2017). Crosstalk between the nucleolus and the DNA damage response. *Mol Biosyst* 13, 443-455.

Palm, W., Park, Y., Wright, K., Pavlova, N.N., Tuveson, D.A., and Thompson, C.B. (2015). The Utilization of Extracellular Proteins as Nutrients Is Suppressed by mTORC1. *Cell* 162, 259-270.

Paradis, E., and Schliep, K. (2019). ape 5.0: an environment for modern phylogenetics and evolutionary analyses in R. *Bioinformatics* 35, 526-528.

Paraiso, K.H., and Smalley, K.S. (2013). Fibroblast-mediated drug resistance in cancer. *Biochem Pharmacol* 85, 1033-1041.

Parker, J.S., Mullins, M., Cheang, M.C., Leung, S., Voduc, D., Vickery, T., Davies, S., Fauron, C., He, X., Hu, Z., *et al.* (2009). Supervised risk predictor of breast cancer based on intrinsic subtypes. *J Clin Oncol* 27, 1160-1167.

Pauken, K.E., and Wherry, E.J. (2015). Overcoming T cell exhaustion in infection and cancer. *Trends Immunol* 36, 265-276.

Peixoto, L., Risso, D., Poplawski, S.G., Wimmer, M.E., Speed, T.P., Wood, M.A., and Abel, T. (2015). How data analysis affects power, reproducibility and biological insight of RNA-seq studies in complex datasets. *Nucleic Acids Res* 43, 7664-7674.

Riesterer, J.L., Lopez, C.S., Stempinski, E.S., Williams, M., Loftis, K., Stoltz, K., Thibault, G., Lanicault, C., Williams, T., and Gray, J.W. (2020). A workflow for visualizing human cancer biopsies using large-format electron microscopy. *Methods Cell Biol* 158, 163-181.

Risso, D., Ngai, J., Speed, T.P., and Dudoit, S. (2014). Normalization of RNA-seq data using factor analysis of control genes or samples. *Nat Biotechnol* 32, 896-902.

Robinson, D.R., Wu, Y.M., Vats, P., Su, F., Lonigro, R.J., Cao, X., Kalyana-Sundaram, S., Wang, R., Ning, Y., Hodges, L., *et al.* (2013). Activating ESR1 mutations in hormone-resistant metastatic breast cancer. *Nat Genet* 45, 1446-1451.

Rodchenkov, I., Babur, O., Luna, A., Aksoy, B.A., Wong, J.V., Fong, D., Franz, M., Siper, M.C., Cheung, M., Wrana, M., *et al.* (2020). Pathway Commons 2019 Update: integration, analysis and exploration of pathway data. *Nucleic Acids Res* 48, D489-D497.

Rozenblatt-Rosen, O., Regev, A., Oberdoerffer, P., Nawy, T., Hupalowska, A., Rood, J.E., Ashenberg, O., Cerami, E., Coffey, R.J., Demir, E., *et al.* (2020). The Human Tumor Atlas Network: Charting Tumor Transitions across Space and Time at Single-Cell Resolution. *Cell* 181, 236-249.

Saki, M., and Prakash, A. (2017). DNA damage related crosstalk between the nucleus and mitochondria. *Free Radic Biol Med* 107, 216-227.

Schietinger, A., Philip, M., Krisnawan, V.E., Chiu, E.Y., Delrow, J.J., Basom, R.S., Lauer, P., Brockstedt, D.G., Knoblaugh, S.E., Hammerling, G.J., *et al.* (2016). Tumor-Specific T Cell Dysfunction Is a Dynamic Antigen-Driven Differentiation Program Initiated Early during Tumorigenesis. *Immunity* 45, 389-401.

Sherr, C.J., Beach, D., and Shapiro, G.I. (2016). Targeting CDK4 and CDK6: From Discovery to Therapy. *Cancer Discov* 6, 353-367.

Soneson, C., Love, M.I., and Robinson, M.D. (2016). Differential analyses for RNA-seq: transcript-level estimates improve gene-level inferences. *F1000 Res* 5, 1-21.

Spring, L.M., Wander, S.A., Andre, F., Moy, B., Turner, N.C., and Bardia, A. (2020). Cyclin-dependent kinase 4 and 6 inhibitors for hormone receptor-positive breast cancer: past, present, and future. *Lancet* 395, 817-827.

Tai, P., Wang, J., Jin, H., Song, X., Yan, J., Kang, Y., Zhao, L., An, X., Du, X., Chen, X., *et al.* (2008). Induction of regulatory T cells by physiological level estrogen. *J Cell Physiol* 214, 456-464.

Talevich, E., Shain, A.H., Botton, T., and Bastian, B.C. (2016). CNVkit: Genome-Wide Copy Number Detection and Visualization from Targeted DNA Sequencing. *PLoS Comput Biol* 12, e1004873.

Tatlow, P.J., and Piccolo, S.R. (2016). A cloud-based workflow to quantify transcript-expression levels in public cancer compendia. *Sci Rep* 6, 39259.

Tibes, R., Qiu, Y., Lu, Y., Hennessy, B., Andreeff, M., Mills, G.B., and Kornblau, S.M. (2006). Reverse phase protein array: validation of a novel proteomic technology and utility for analysis of primary leukemia specimens and hematopoietic stem cells. *Mol Cancer Ther* 5, 2512-2521.

Toy, W., Shen, Y., Won, H., Green, B., Sakr, R.A., Will, M., Li, Z., Gala, K., Fanning, S., King, T.A., *et al.* (2013). ESR1 ligand-binding domain mutations in hormone-resistant breast cancer. *Nat Genet* 45, 1439-1445.

Tsujikawa, T., Kumar, S., Borkar, R.N., Azimi, V., Thibault, G., Chang, Y.H., Balter, A., Kawashima, R., Choe, G., Sauer, D., *et al.* (2017). Quantitative Multiplex Immunohistochemistry Reveals Myeloid-Inflamed Tumor-Immune Complexity Associated with Poor Prognosis. *Cell Rep* 19, 203-217.

Tsujikawa, T., Thibault, G., Azimi, V., Sivagnanam, S., Banik, G., Means, C., Kawashima, R., Clayburgh, D.R., Gray, J.W., Coussens, L.M., *et al.* (2019). Robust Cell Detection and Segmentation for Image Cytometry Reveal Th17 Cell Heterogeneity. *Cytometry A* 95, 389-398.

Vilgelm, A.E., Saleh, N., Shattuck-Brandt, R., Riemenschneider, K., Slesur, L., Chen, S.C., Johnson, C.A., Yang, J., Blevins, A., Yan, C., *et al.* (2019). MDM2 antagonists overcome intrinsic resistance to CDK4/6 inhibition by inducing p21. *Sci Transl Med* 11.

Villamil Giraldo, A.M., Appelqvist, H., Ederth, T., and Ollinger, K. (2014). Lysosomotropic agents: impact on lysosomal membrane permeabilization and cell death. *Biochem Soc Trans* 42, 1460-1464.

Wagner, A.H., Walsh, B., Mayfield, G., Tamborero, D., Sonkin, D., Krysiak, K., Deu-Pons, J., Duren, R.P., Gao, J., McMurry, J., *et al.* (2020). A harmonized meta-knowledgebase of clinical interpretations of somatic genomic variants in cancer. *Nat Genet* 52, 448-457.

Wculek, S.K., Cueto, F.J., Mujal, A.M., Melero, I., Krummel, M.F., and Sancho, D. (2020). Dendritic cells in cancer immunology and immunotherapy. *Nat Rev Immunol* 20, 7-24.

Wijayarathne, A.L., and McDonnell, D.P. (2001). The human estrogen receptor- α is a ubiquitinated protein whose stability is affected differentially by agonists, antagonists, and selective estrogen receptor modulators. *J Biol Chem* 276, 35684-35692.

Wittmann, B.M., Sherk, A., and McDonnell, D.P. (2007). Definition of functionally important mechanistic differences among selective estrogen receptor down-regulators. *Cancer Res* 67, 9549-9560.

Wolf, F.A., Angerer, P., and Theis, F.J. (2018). SCANPY: large-scale single-cell gene expression data analysis. *Genome Biol* 19, 15.

Young Hwan, C., Thibault, G., Madin, O., Azimi, V., Meyers, C., Johnson, B., Link, J., Margolin, A., and Gray, J.W. (2017). Deep learning based Nucleus Classification in pancreas histological images. *Annu Int Conf IEEE Eng Med Biol Soc 2017*, 672-675.

Figure 1

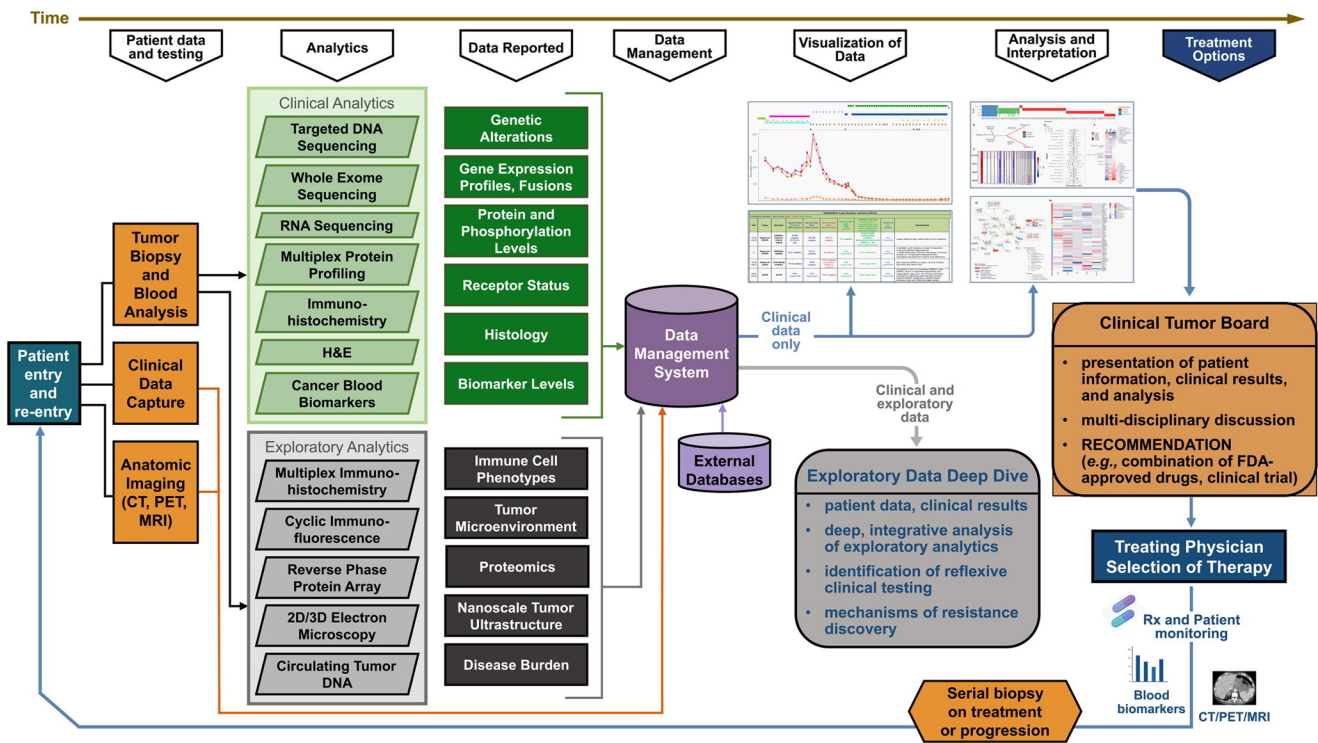


Figure 2

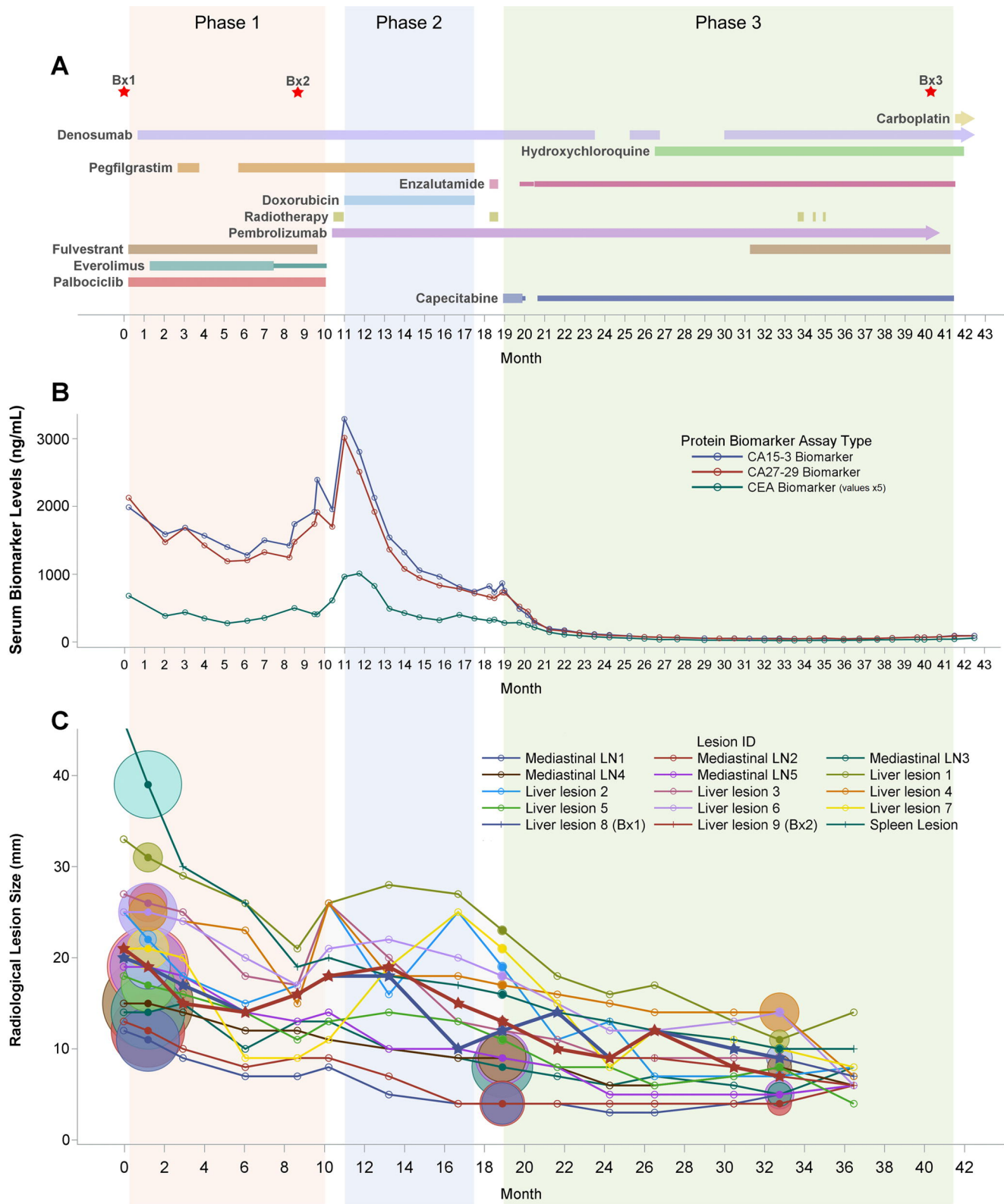


Figure 3

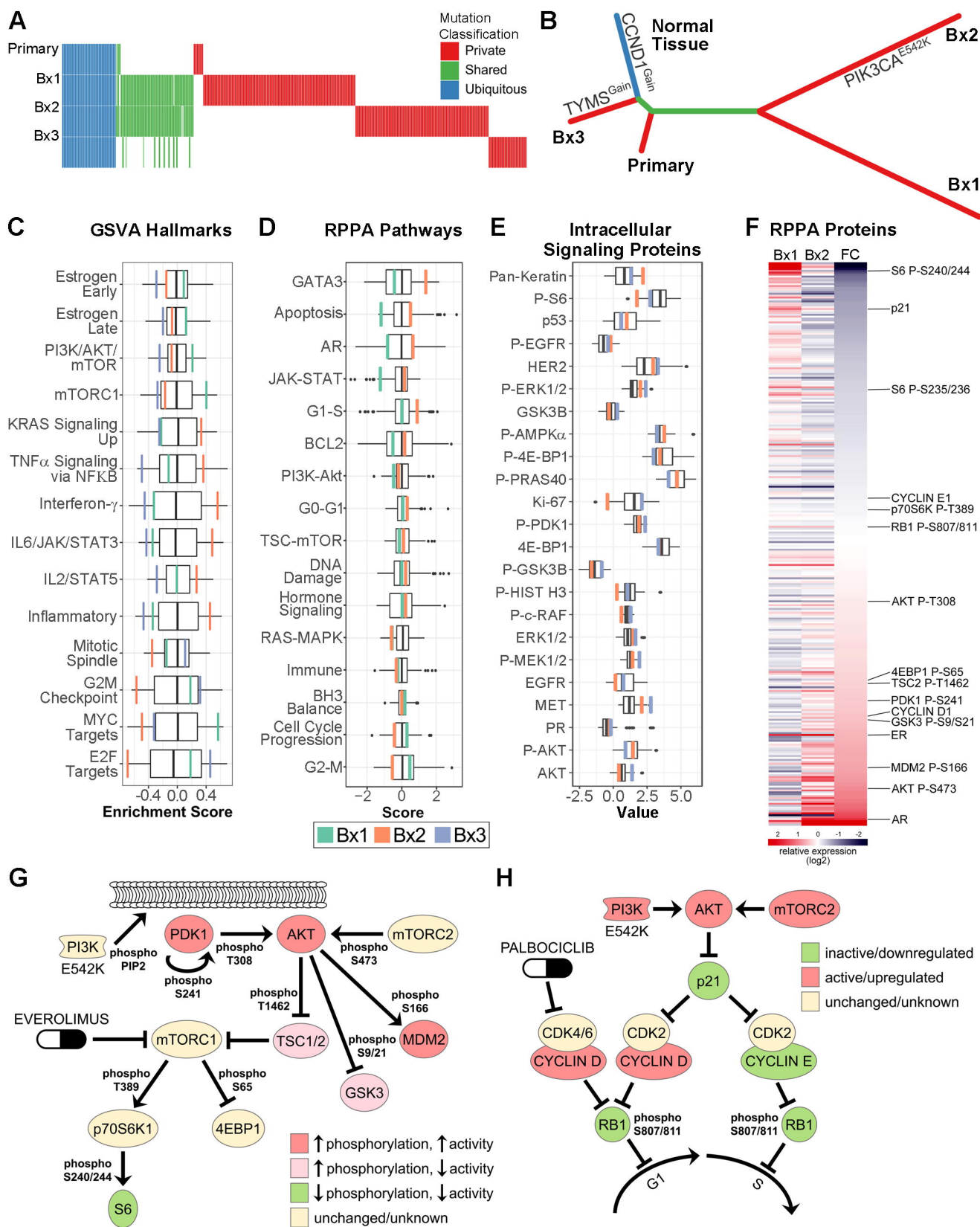


Figure 4

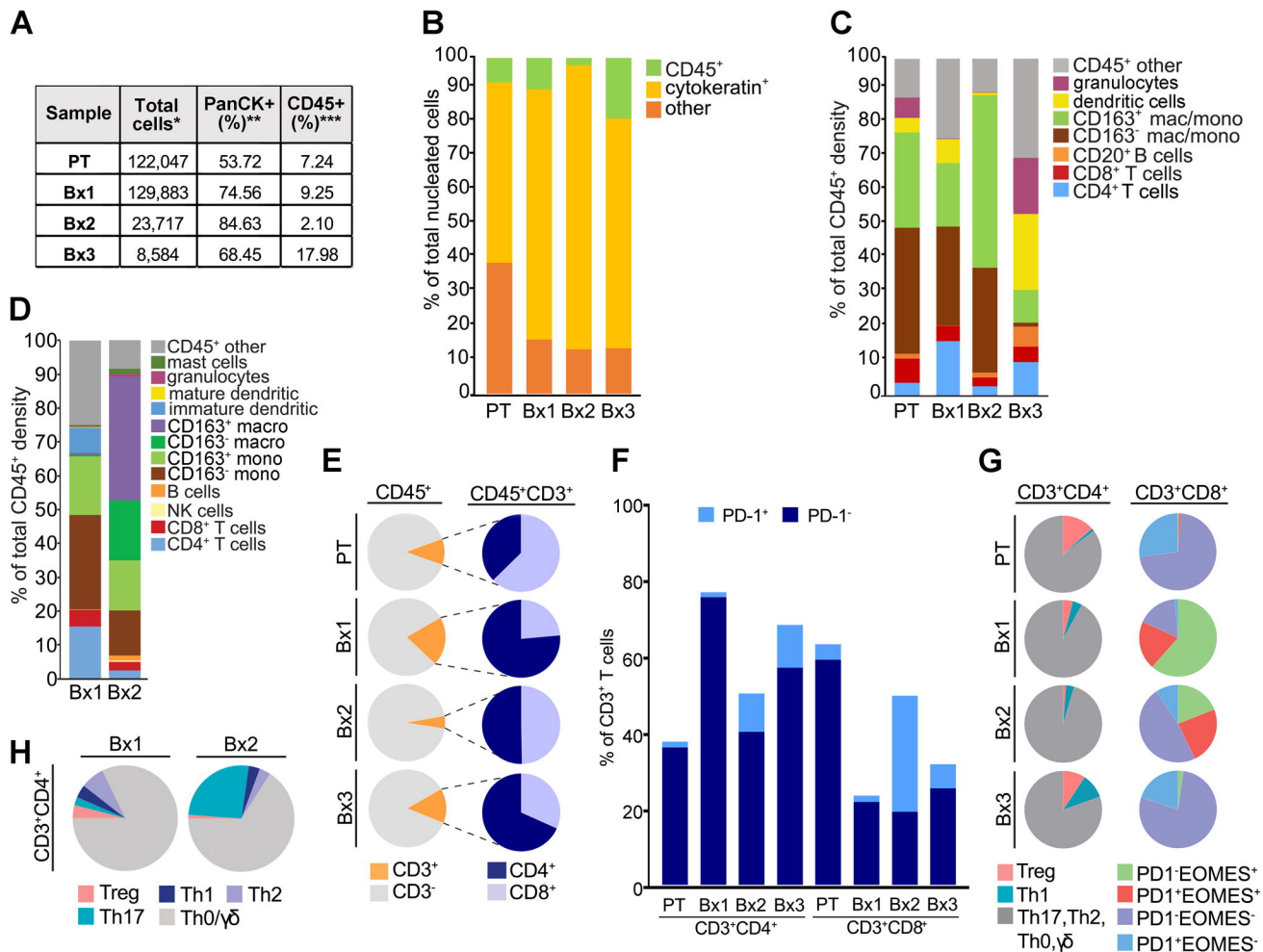


Figure 5

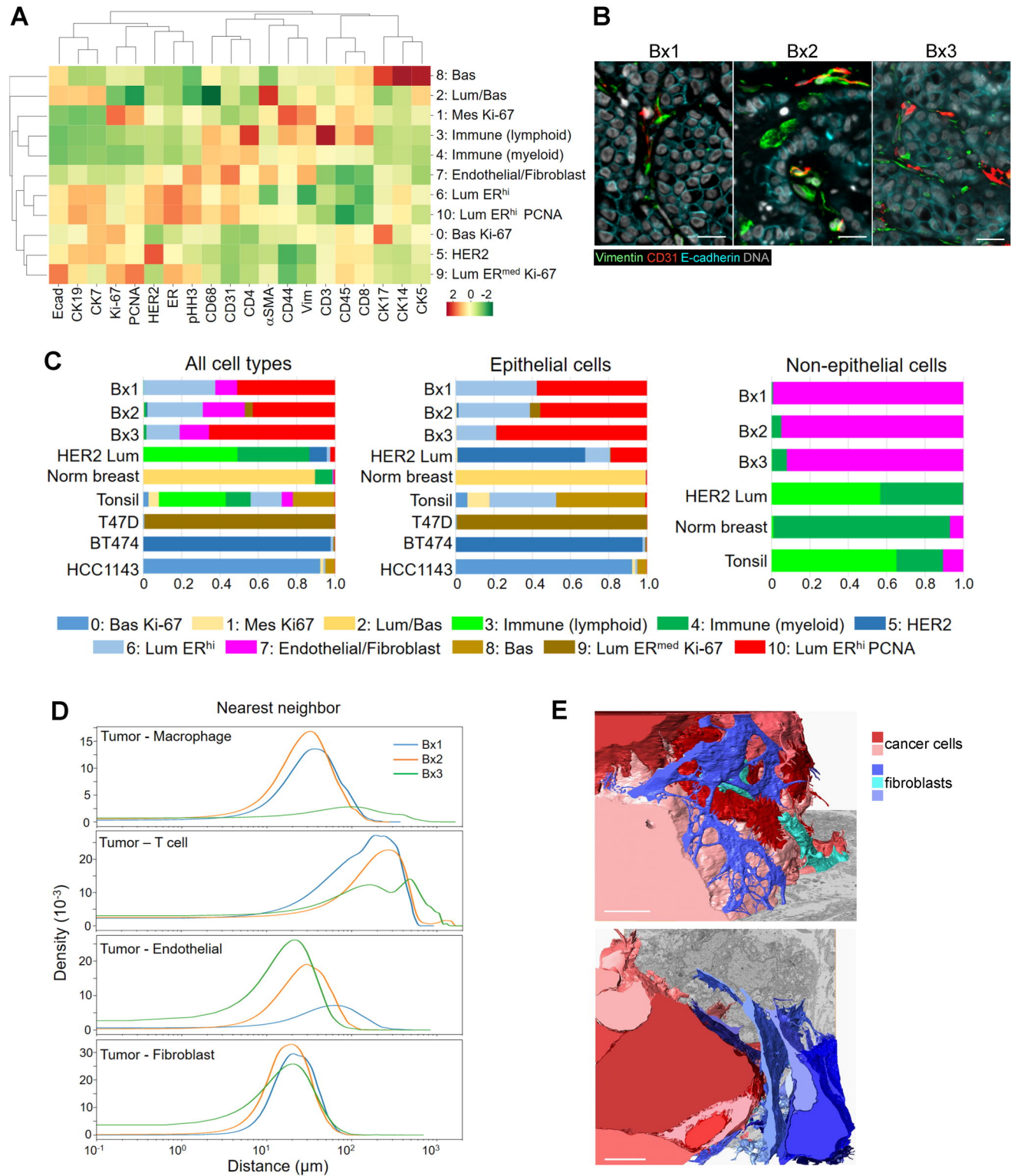


Figure 6

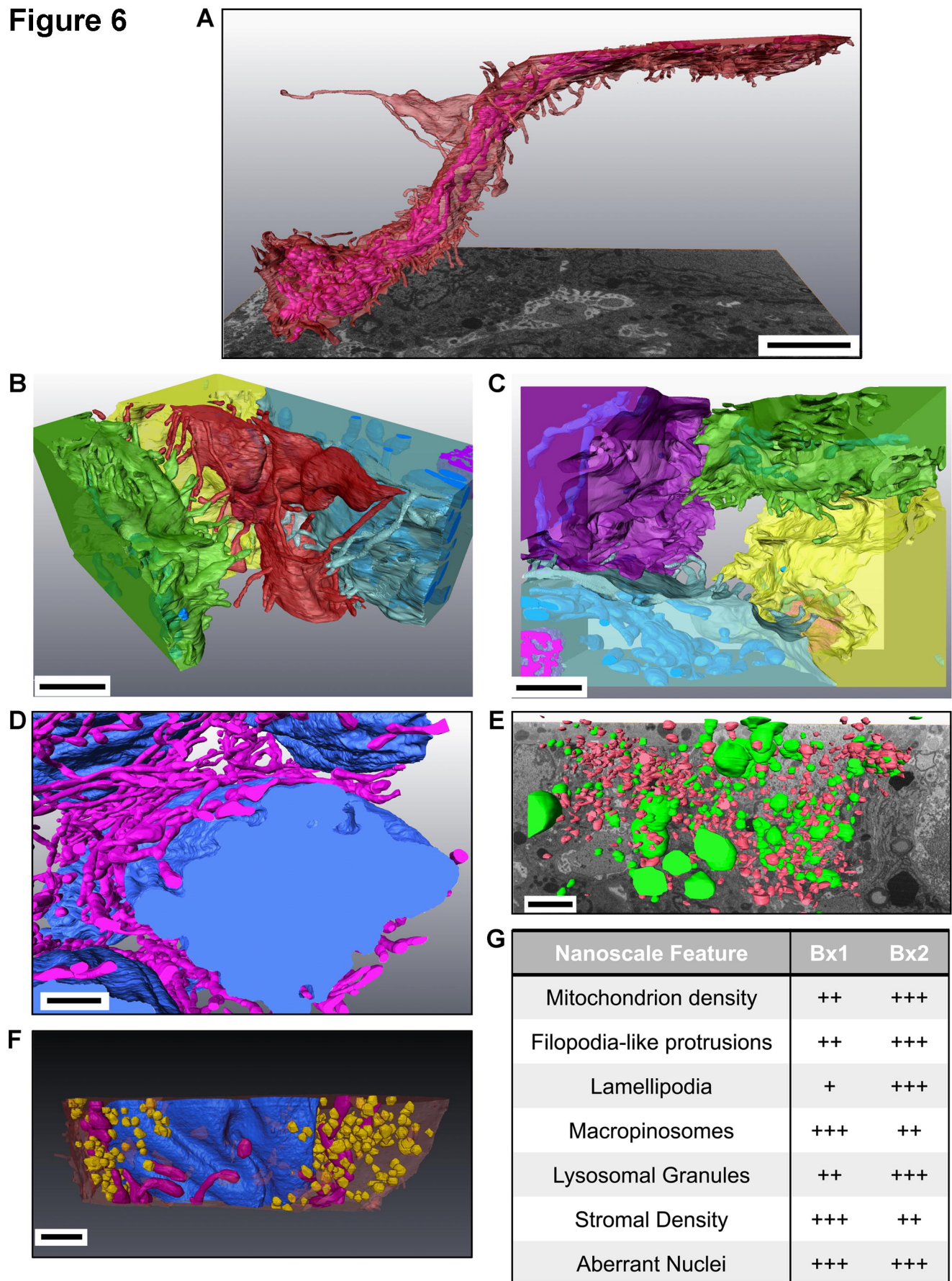


Figure S1

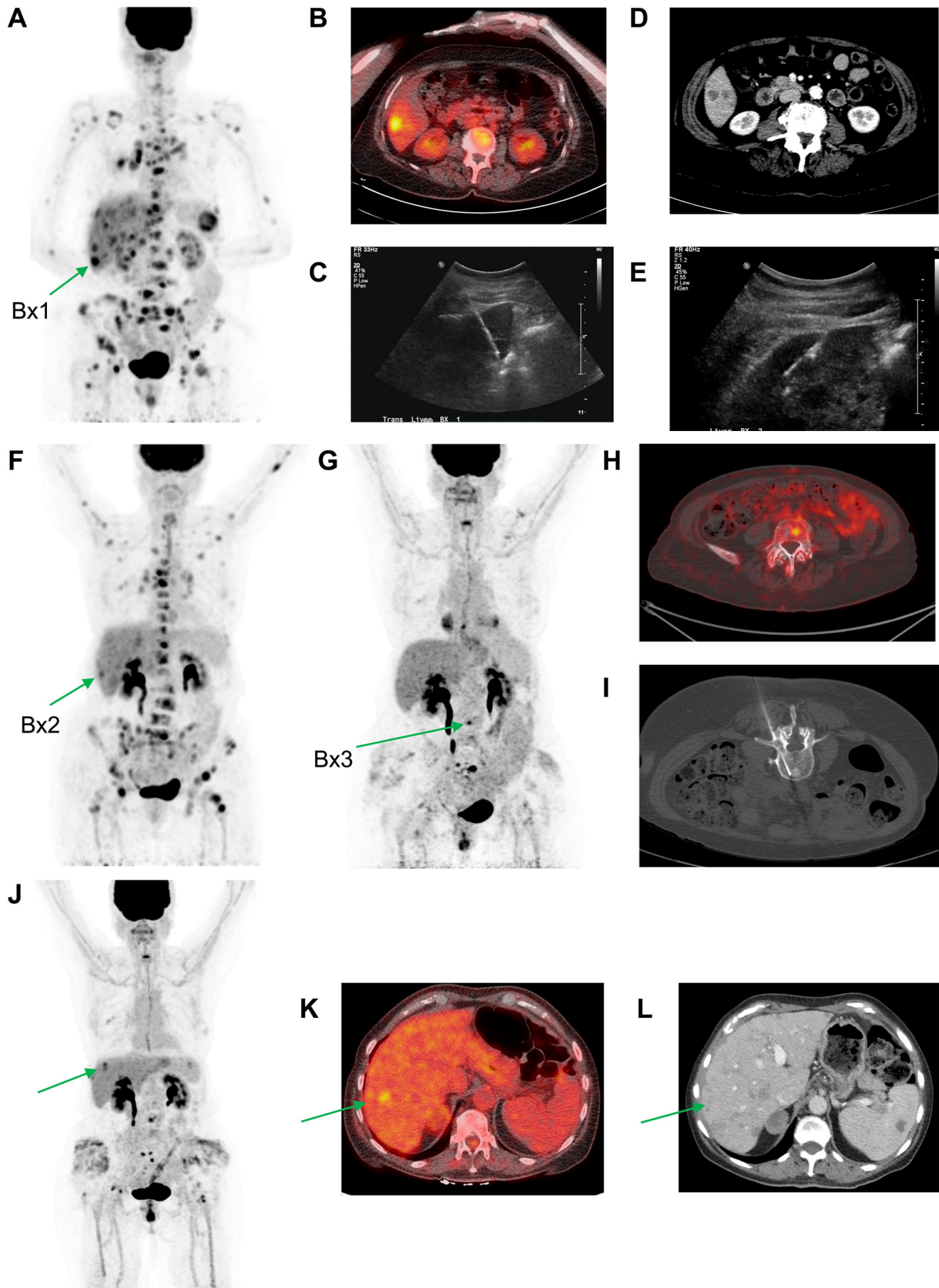


Figure S2

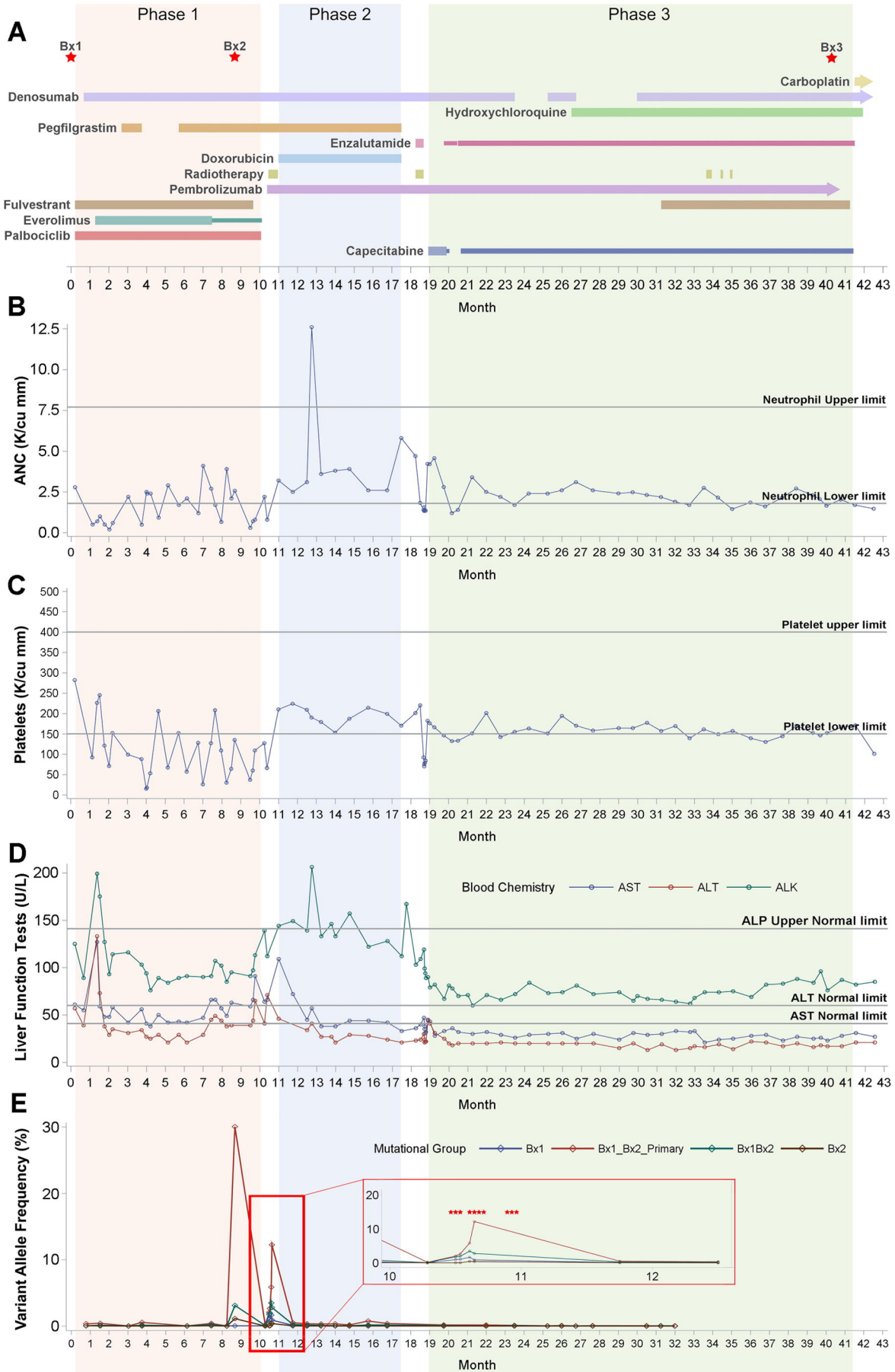


Figure S3

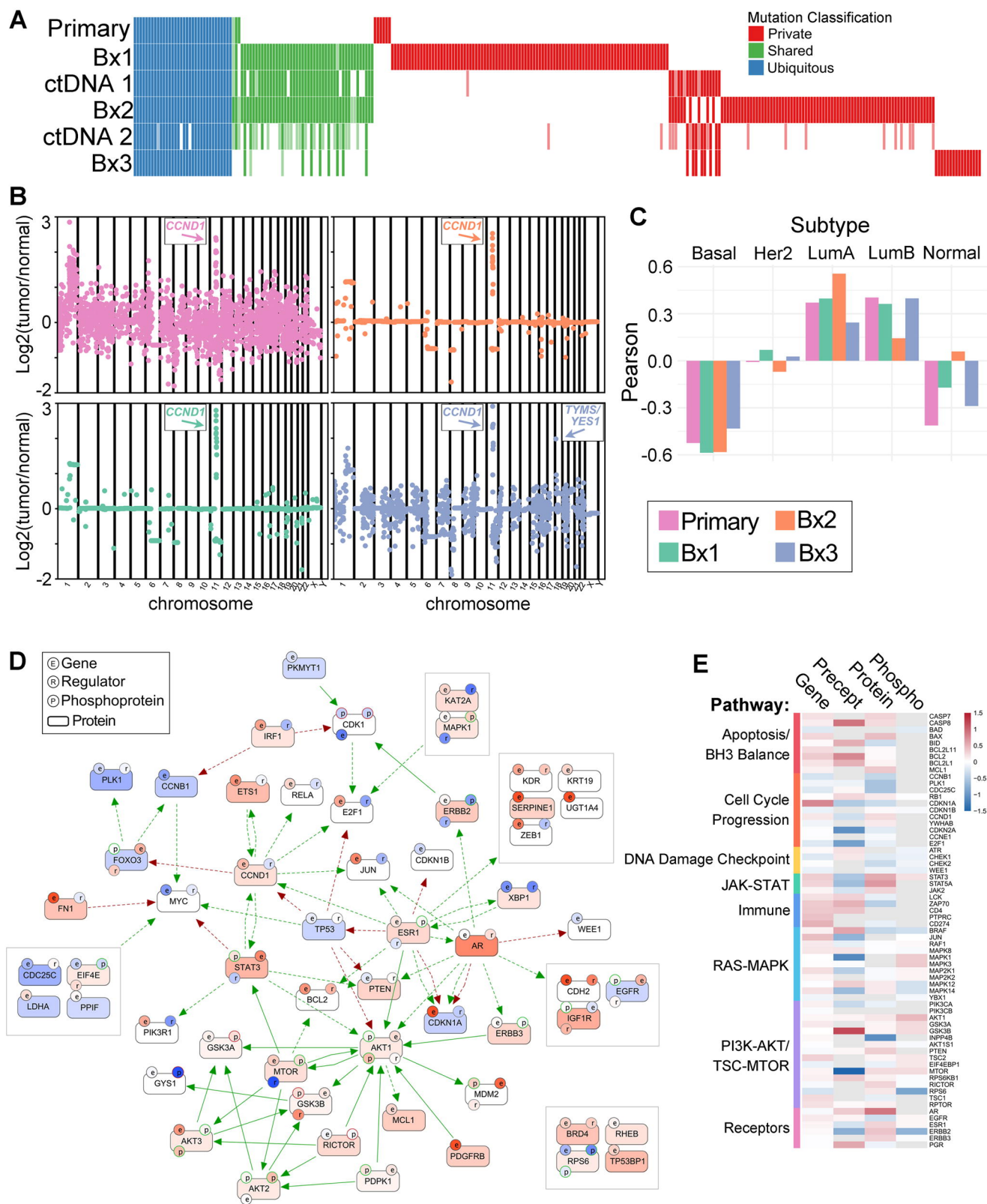


Figure S4

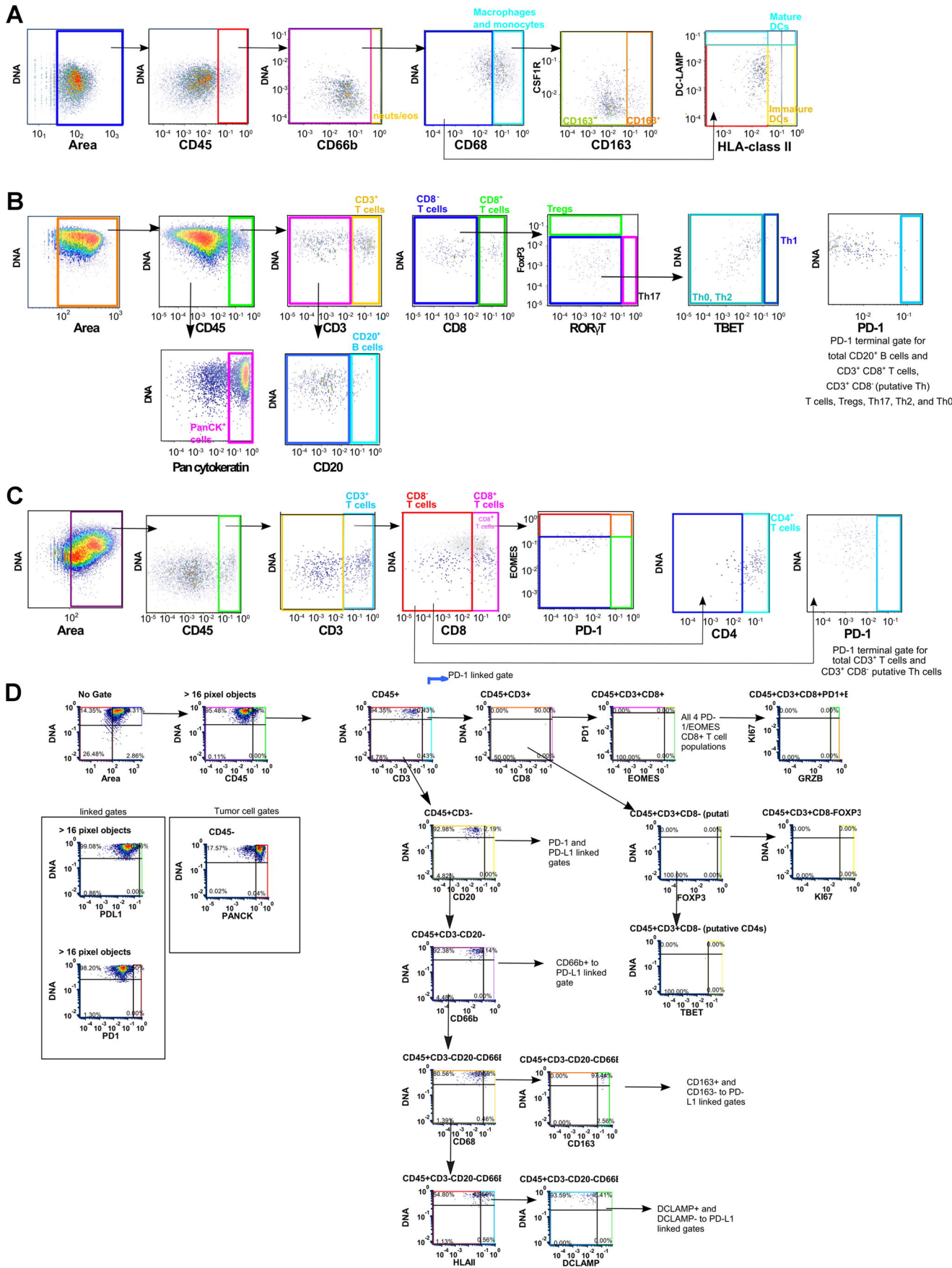


Figure S5

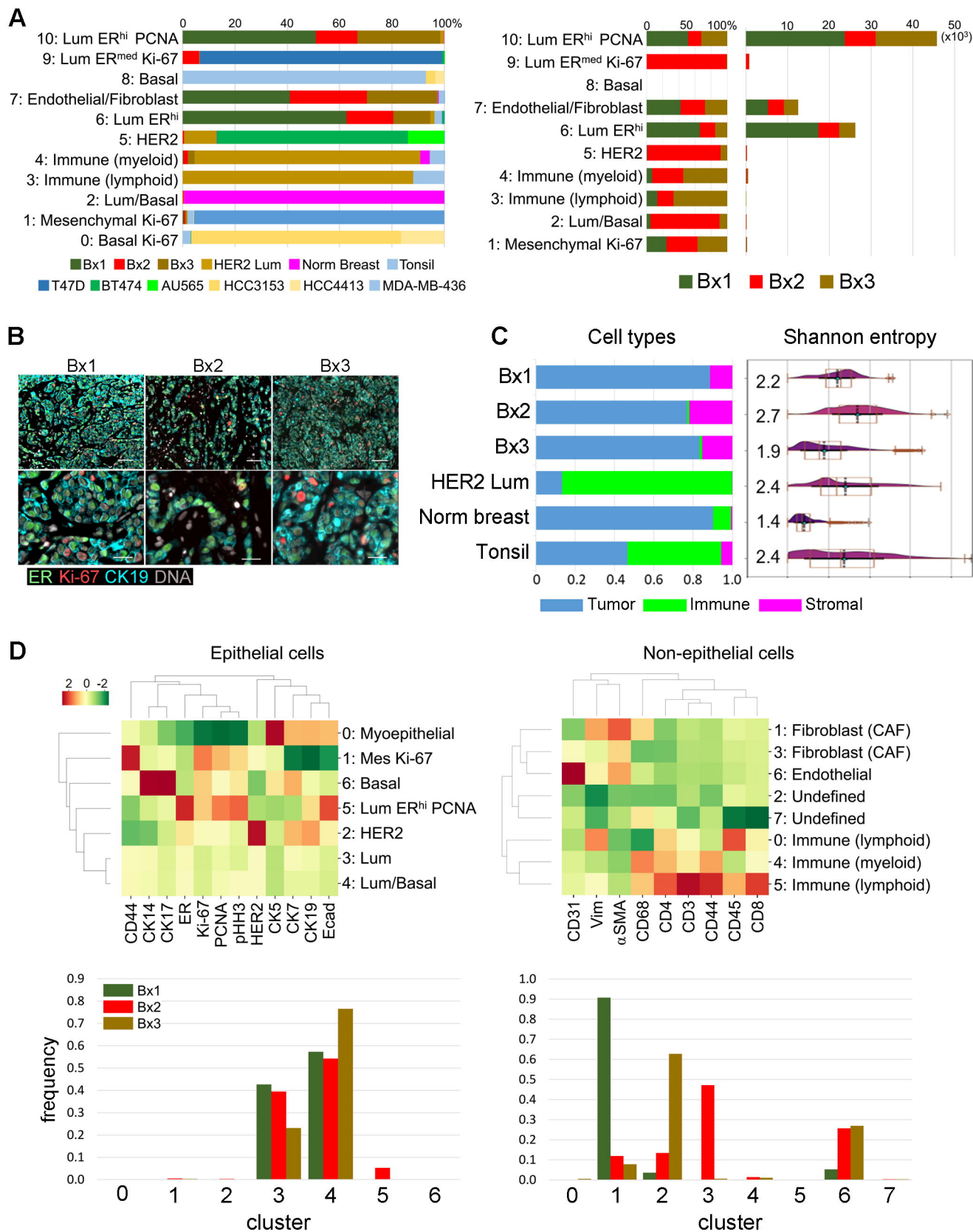


Figure S6

